4-2020

Development of a Finite Element Model of the Stamping Process to Predict the Natural Frequencies of Dimpled Beams

Varad Vasudeo Pendse
Western Michigan University, varadpondse@gmail.com

DEVELOPMENT OF A FINITE ELEMENT MODEL OF THE STAMPING PROCESS TO PREDICT THE NATURAL FREQUENCIES OF DIMPLED BEAMS

by

Varad Vasudeo Pendse

A thesis submitted to the Graduate College
in partial fulfilment of the requirements
for the degree of Master of Science in Engineering (Mechanical)
Mechanical and Aerospace Engineering
Western Michigan University
April 2020

Thesis Committee:

Koorosh Naghshineh, Ph.D., Chair
Judah Ari-Gur, D.Sc.
Richard Meyer, Ph.D.

DEVELOPMENT OF A FINITE ELEMENT MODEL OF THE STAMPING PROCESS TO PREDICT THE NATURAL FREQUENCIES OF DIMPLED BEAMS

Varad Vasudeo Pendse, M.S.E.

Western Michigan University, 2020

Creating dimples on beams has been proven to be an effective way of altering their vibrational behavior. The objective of this research is to simulate the process of stamping using the finite element (FE) method to create a model of a dimpled beam. This dimple has non-uniform thickness, so it shows close agreement with its real-life counterpart.

ANSYS® Parametric Design Language (APDL) is used to build a three-dimensional (3-D) finite element model and simulate the process of stamping used to create the dimple. The structural simulation is validated by calculating the thickness and width of the deformed geometry of the FE beam and comparing these calculations to measurements of thickness and width made on an experimental dimpled beam. Further, natural frequencies of a beam with a single dimple, a beam with two dimples in the same direction, and a beam with two dimples in opposite directions are extracted for free-free boundary conditions from this FE model. They are then compared with results from the experimental modal analysis of beams with the same geometry and boundary conditions. This comparison yields an average accuracy of 0.71% for the FEA results, pointing to excellent agreement between both sets of data.

ACKNOWLEDGEMENTS

Sir Isaac Newton once remarked “If I have seen further, it is by standing on the shoulders of giants”. And while the research presented here is insignificant next to the work of that scientific luminary, I share his sentiment as I thank all the people who helped me in this project.

First and foremost, I owe a debt of gratitude to my advisor, Dr. Koorosh Naghshineh for his motivating and immensely helpful nature. I am thankful as well to the members of my thesis committee, Dr. Judah Ari-Gur and Dr. Richard Meyer for their insightful comments and suggestions. Also, thanks to Dr. Nabeel Alshabtat and Dr. Kyle Myers who previously explored this subject and whose work laid the foundations I built upon. I am deeply obliged to Mofareh Ghazwani who, in addition to expanding Dr. Myers’ work, helped me understand it and generated numerous results for comparison with my work. A special thanks to Mike Konkel and Allin Kahrl for machining the test specimens for tension testing, and to Dr. Daniel Kujawski and Suraj Nikam, for taking time out of their busy research schedules to conduct the tension tests.

Most of this work could not have been completed without the use of ANSYS Parametric Design Language (APDL) and MATLAB, robust and sophisticated software developed by ANSYS, Inc. and MathWorks respectively. I am grateful to Dr. Mitchell Keil for scanning the beams and Dr. Ramona Lewis for arranging the Graduate Summer Writing Experience which jumpstarted the process of writing this thesis.

Last but undoubtedly not the least, I am forever indebted to my parents, Vasudeo and Vrunda, and the rest of my family for their unconditional support. I am also thankful to my friends who kept me on track and have lent a helping hand in more ways than I can count.

Varad Vasudeo Pendse

TABLE OF CONTENTS

LIST OF TABLES

LIST OF FIGURES

1. Introduction and literature review

There has been considerable research about altering the vibroacoustic behavior of beams and plates. Of the methods studied, stamping and beading of beams and plates is one which achieves this without adding mass to the underlying structure. Simulation of such dimpled beams is an objective of this research and this chapter lays the groundwork for the work explained in subsequent chapters. Section 1.1 describes attempts to minimize sound radiation of structures by methods other than dimpling. Section 1.2 follows with an introduction to dimples and beads, while Section 1.3 provides an overview of the relevant research. Section 1.4 establishes the need and consequent motivation for this work and Section 1.5 ends the chapter with a description of the remainder of the work.

1.1. Preface

Minimizing the sound radiation of structures has been an area of interest over the past decades and minimizing vibrations has often been proposed as the starting point. Solutions suggested range from the outright addition of mass to the structure to the use of vibration absorbers [1], topology optimization [2], addition of stiffeners [3], or even some combination of these.

Naghshineh [4] aimed to alter structures and turn them into what he termed 'weak radiators' by minimizing their radiated sound power. Two approaches were suggested to achieve this – passively changing the structure's material properties or actively changing its vibration response. The latter of the two has been a past topic of research [5], [6], [7] and is also a point of interest here.

1.2. Introduction to dimples and beads

The structures described in the next section are limited to beams and plates. Altering their vibrational behavior is achieved by creating dimples and beads on them via the process of stamping. It is a proven method of changing natural frequencies and mode shapes of the underlying structure. Further, it is a one-step process that is cost-effective and easy to execute.

Dimples are defined as partially circular deformations and are of two kinds depending on the type of structure they are made on. In the context of plates, dimples are spherical segments, while they are cylindrical segments when created on a beam. A bead is a partially cylindrical deformation with spherical ends uniquely applied to a plate geometry. Figure 1.1 *Plate with a bead in the center and spherical dimples at four points around it*

Figure 1.2 Beam with two cylindrical dimples pointing in opposite directionsFigure 1.1 shows a plate with a bead and four spherical dimples, while Figure 1.2 *Beam with two cylindrical dimples pointing in opposite directions* shows a beam with two cylindrical dimples pointing in opposite directions. As the present research deals solely with beams, cylindrical dimples (such as those shown in Figure 1.2 *Beam with two cylindrical dimples pointing in opposite directions*) are the only ones that are relevant and will be referred to as simply 'dimples' in the sequel.

1.3. Overview of relevant research

Cheng *et al.* [8] proposed strategically placing cylindrical dimples on a beam such that its mode shapes correspond to the mode shapes of a weak radiator ('weak modes'). They employed the finite element method to calculate these weak modes and then used an optimization algorithm to determine the location of dimples and other parameters such as angle and depth. The radiation efficiency of dimpled beams produced in this way was shown to be lower than that of a uniform beam. It was also noted that the effectiveness of this procedure depended on the agreement between the mode shapes of the dimpled beam and the corresponding weak modes.

Alshabtat [5] advanced this research by investigating the effects of dimples and beads on the vibroacoustic behavior of beams and plates. The objectives were twofold – first, the optimization of natural frequencies of beams and plates and second, the minimization of sound radiated from vibrating plates. Simulating the vibrations of these structures using finite element software showed that the changes in natural frequencies of dimpled beams depended to a large extent on the boundary conditions implemented. He surmised that these changes were the result of a change in the beams' bending stiffness and that this change was governed by two effects, namely the thinning effect and the curvature effect. The deformation occurring through the

process of stamping decreases the beam's thickness which, in turn, decreases its bending stiffness as well. On the other hand, the curvature effect couples the axial and transverse motions of the beam. This means that an axially unconstrained beam has only the thinning effect at work and has a decreased bending stiffness. Conversely, if a beam is axially constrained, its bending stiffness might increase or decrease depending on which of the thinning or curvature effects is dominant. Alshabtat also replicated these studies for plates by placing dimples and beads at different locations and observing changes in their vibrational behavior. Additionally, an optimization technique known as the Genetic Algorithm (GA) was used to optimize the placement of beads and dimples on plates with the objective of minimizing its sound power.

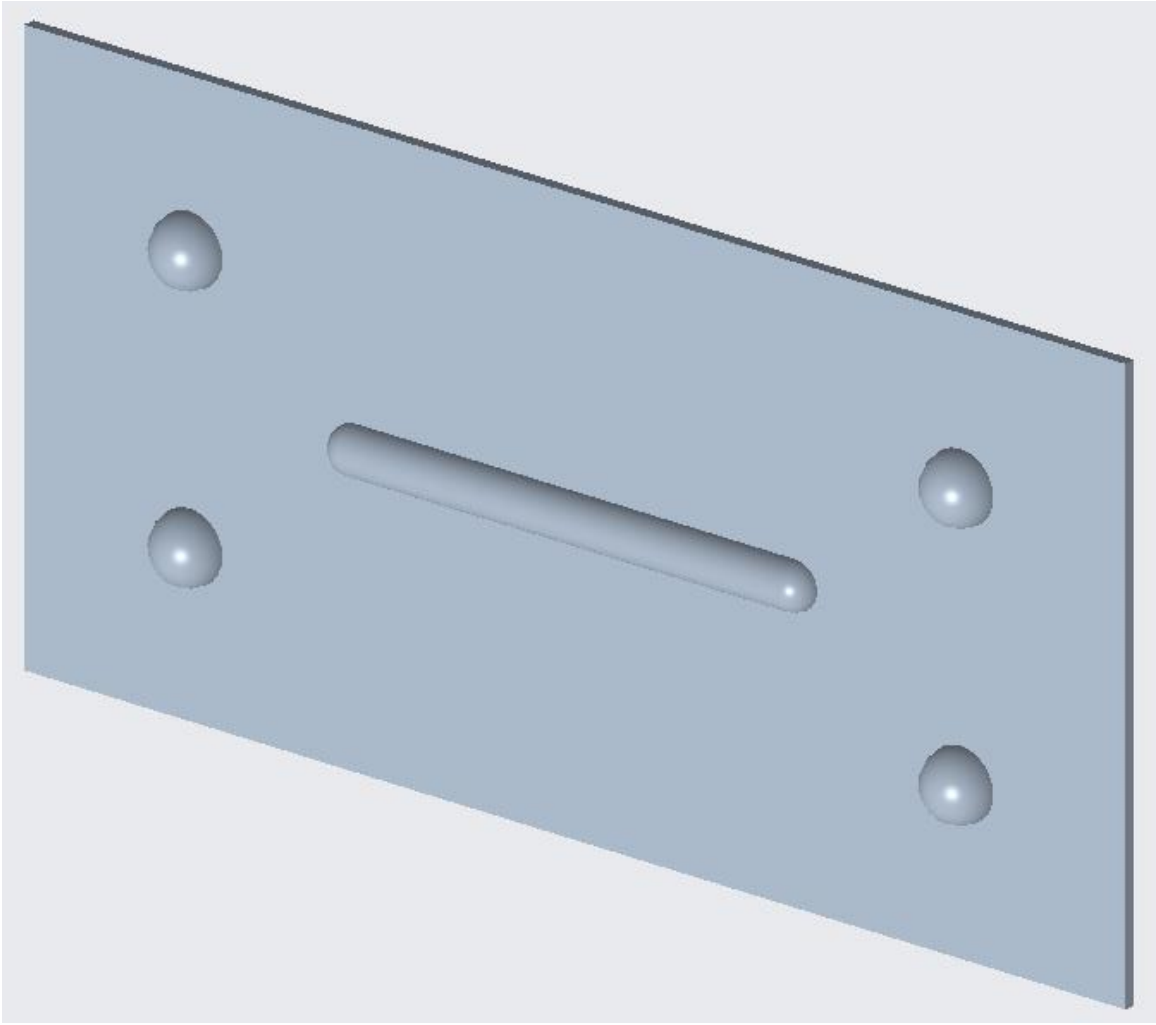

Figure 1.1 Plate with a bead in the center and spherical dimples at four points around it

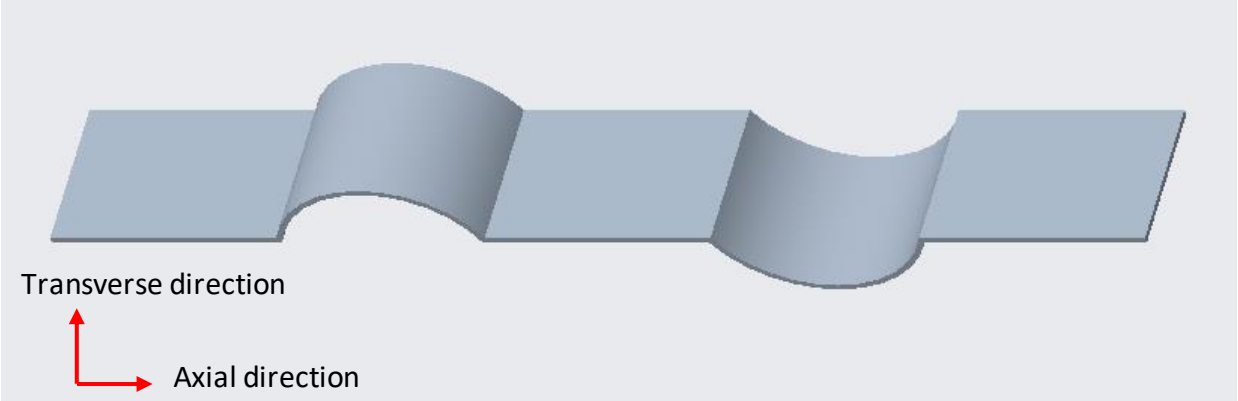

Figure 1.4 Beam with two cylindrical dimples pointing in opposite directions

Myers [6] developed a boundary value model (BVM) for a beam with a single dimple using Hamilton's Variational Principle. Unlike Cheng [8] and Alshabtat [5], he undertook mathematical formulations to analytically model a dimpled beam as a series of straight beams and arches. These straight beams and arches were connected using continuity and equilibrium conditions. These conditions were also satisfied by the differential equation of motion derived to describe the axial and transverse vibrations of the beam. This model also accounted for the extension of the dimple along its circumference and resulting thinning.

Myers also investigated the effects of dimple placement, dimple angle, chord length, thickness and boundary conditions on the beam natural frequencies and mode shapes. He showed that dimples placed at locations of high modal strain energy (MSE) were more sensitive to changes in dimple angle as compared to those placed at locations of zero MSE. Based on this, MSE was proposed as a possible design variable in determining optimal dimple location. With dimple location determined by MSE, an optimization algorithm could then be used to determine the dimple angle. The feasibility of this design strategy was demonstrated by using MSE with the genetic algorithm to maximize the fundamental frequency of a fixed-fixed beam with two dimples. Further study was conducted on the effect of dimpling on sound radiation as compared to uniform beams.

Ghazwani [7] worked along similar lines and developed a BVM for beams with two dimples. He considered several boundary conditions to evaluate the effect of dimple orientation

on the vibrational characteristics of the beam. He found significant differences in the vibrational behavior of the beam when both dimples faced the same way in contrast to when they pointed in opposite directions.

1.4. Research motivation

A vital observation shared by all these studies concerns the thickness of the dimples. While stamping manages to affect the vibroacoustic characteristics of beams without adding mass, it does so by reducing beam thickness in the region of the dimple. In previous research [5], [6], [7], the effect of this reduction is accounted for, by assuming a reduced but uniform dimple thickness. Differences greater than 10% were observed in natural frequencies calculated by mathematical models when compared with those obtained from experimental modal analyses. Among other reasons, this assumption of uniform dimple thickness is also used to explain these discrepancies. Figure 1.3 *Comparison of dimple with uniform thickness (left) and dimple with non-uniform thickness (right)* shows a dimple with uniform thickness as assumed by the theoretical studies along with a depiction of the dimple showing variations in its thickness.

Figure 1.5 Comparison of dimple with uniform thickness (left) and dimple with non-uniform thickness (right)

Given these past discrepancies in frequencies and the use of simplifying assumptions, there is a clear need to study the effects of stamping on the natural frequencies of dimpled beams and the present research aims to address that need. First off, a finite element (FE) model of the process of stamping will be developed that will yield a FE version of the dimpled beam. This FE dimpled beam is intended to show variations in thickness like the ones observed in its real-life counterpart. The structural simulation will be validated by comparing it with measurements of thickness made on the real beam. A FE modal analysis will then be conducted to extract its natural frequencies, which will be validated by comparing its results with those from an experimental modal analysis.

1.5. Research organization

The stamping setup used to create the dimples is elaborated on, in Chapter 2. A uniaxial tension test carried out to gain knowledge of the stress-strain behavior of the beam material is described in Chapter 3. The FE simulation of the process of stamping is detailed in Chapter 4. Measurements made on the real dimpled beam and their use to validate the previously developed FE model is explained in Chapter 5. Once the validity of the structural simulation is demonstrated, the modal analysis procedures for the FE dimpled beam and its experimental equivalent are expounded in Chapters 6 and 7. Next, the level of agreement between these two sets of data is evaluated and commented on in Chapter 8. Finally, the findings are summarized, and potential future work is provided in Chapter 9.

2. Stamping setup

This chapter presents the physical stamping setup used to create dimples on the beam from theoretical and practical standpoints. Section 2.1 covers the fundamental mathematical relations between the dimple parameters, which are used later to simulate stamping using finite element (FE) software. Section 2.1 provides a brief theoretical background. Section 2.2 illustrates the stamping setup in detail and provides some insights into the differences between dimples created using this setup and the ones modelled in earlier theoretical works [5], [6], [7]. Section 2.3 summarizes the advantages and disadvantages of the stamping setup.

2.1. Theory

The dimple is created by a plunger coming down on a flat strip of metal. During this process, the elastic limit of the beam material is surpassed, and it undergoes plastic deformation. Initially, the dimple has about the same radius as the plunger. However, after the plunger retracts, uneven elastic recovery occurs along the dimple and its shape ceases to conform to a circular arc. Its height (h), chord length (l) and angle (α) are decided by the distance the plunger travels down. The relationship between the radius, height, chord length and angle of the dimple is governed by basic trigonometry (shown in Figure 2.1 *Trigonometry of a dimple*

Figure 2.2 Dimensions of the stamping setup (All dimensions in mm. Not to scale)Figure 2.1) and hence, once the values for two of these variables are selected, the remaining two are automatically determined.

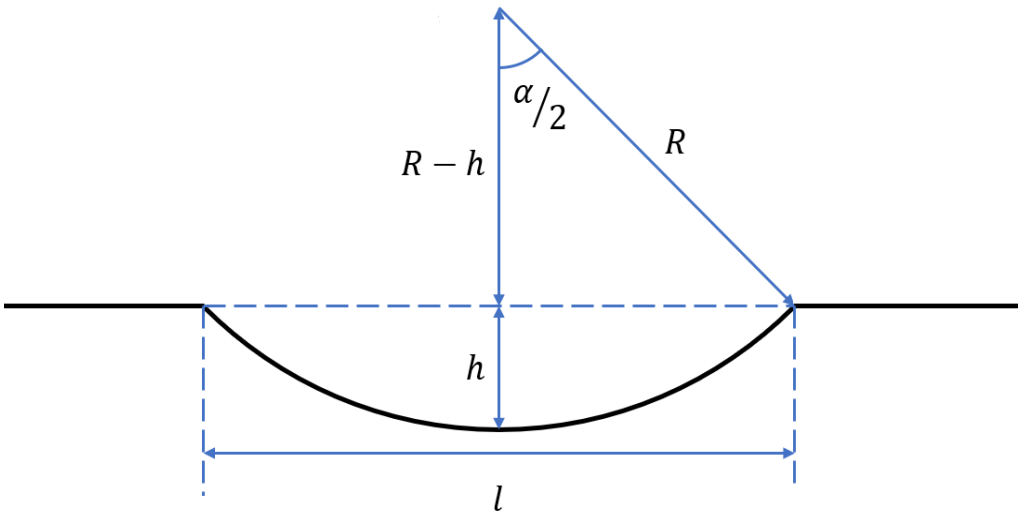

Figure 2.1 Trigonometry of a dimple

From Figure 2.1 *Trigonometry of a dimple*

Figure 2.2 Dimensions of the stamping setup (All dimensions in mm. Not to scale)Figure 2.1, where α, R, h and l are the angle, radius, height and chord length of the dimple respectively, the following relationships can be derived.

$$h = R\left(1 - cos\frac{\alpha}{2}\right) \tag{2.1}$$

$$l = 2R\ sin\frac{\alpha}{2} \tag{2.2}$$

2.2. Formation and analysis of the dimple

Figure 2.2 *Dimensions of the stamping setup (All dimensions in mm. Not to scale)* shows the stamping setup consisting of a baseplate, four clamping blocks and a plunger, all made of steel. Two clamping blocks sit on the baseplate with the distance between them being slightly greater than the diameter of the plunger. The beam rests on these blocks, while the other two clamping blocks sit on top of the beam. Clamping pressure is applied by four bolts holding each pair of the blocks together. Figure 2.3 *Stamping process (clockwise from top left)* illustrates the

process of stamping. Once the beam is firmly clamped, the plunger is pushed down by means of a manually operated hydraulic press to create the dimple. This deformation in the beam is permanent and surpasses the elastic limit. Thus, any modeling of this process must consider plastic deformation and the nonlinearities inherent in this process.

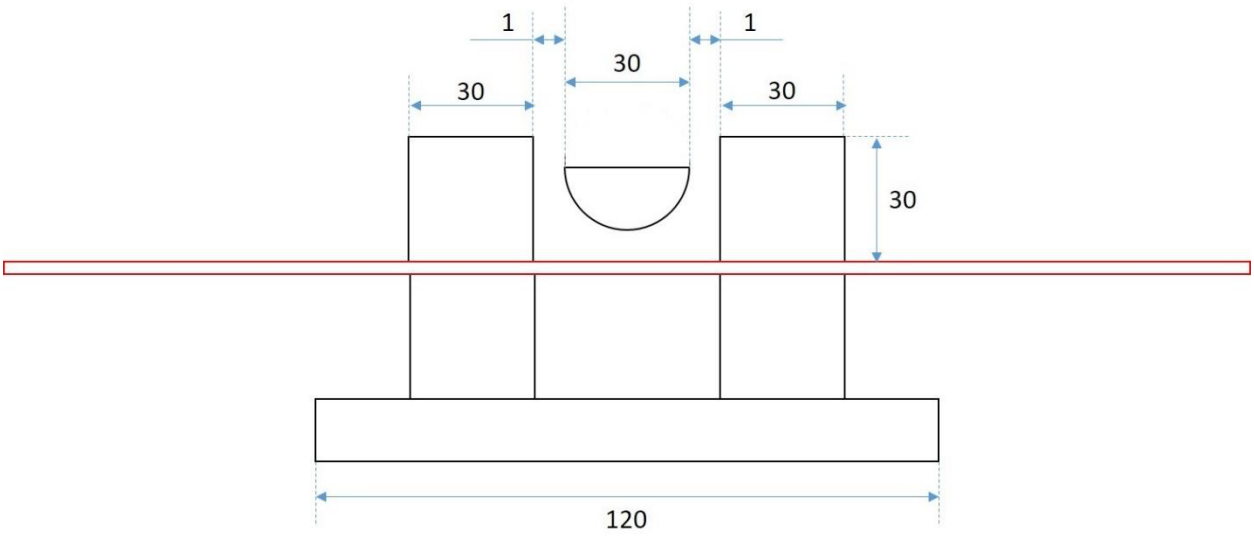

Figure 2.4 Dimensions of the stamping setup (All dimensions in mm. Not to scale)

While the flat beam is uniformly thick and wide, the beam's thickness and width change along the dimple and in its immediate vicinity. These variations in thickness and width are the effect of the beam getting stretched along its length. The strain created along the beam's length causes lateral strains in the directions of its thickness and width. As this strain is the greatest around the dimple's location, this is where the thickness and width are affected the most. Conversely, it is negligible farther away from the dimple and so are the variations in the beam's thickness and width.

To explore this further, a 3-D scan of the beam was performed using an optical coordinate measuring technique. The Advanced Topometric Sensor (ATOS) was used to scan the beam and measure the coordinates of the points on its surface with a high local resolution (0.5 mm) in 3-D space [9]. This set of data was then used to create a point cloud. Plotting this point cloud shows that the change in width is not limited to the dimple alone. Figure 2.4 *Variation in beam width at the dimple and in clamped locations* shows a plot of this data with the beam's length on the

horizontal axis and its width on the vertical. The width can be seen reduced in portions of the beam that would be clamped as well. It is therefore believed that the clamps allow deformation of the beam. The red rectangles are the positions of the clamps, with the red dashed lines indicating the locations where the width can be seen going back to normal. This shows that the clamps allow deformation in their 'inner half', but not in their 'outer half'. While the reasoning for this is unclear and of little relevance to the investigation here, its implications for the deformed shape of the beam are important and examined at a later stage. Unlike the width, changes in thickness are too small to be noticeable to the naked eye. Nevertheless, their presence can be deduced from observations of width (Section 4.6) and proven with the aid of physical measurements (Section 5.3).

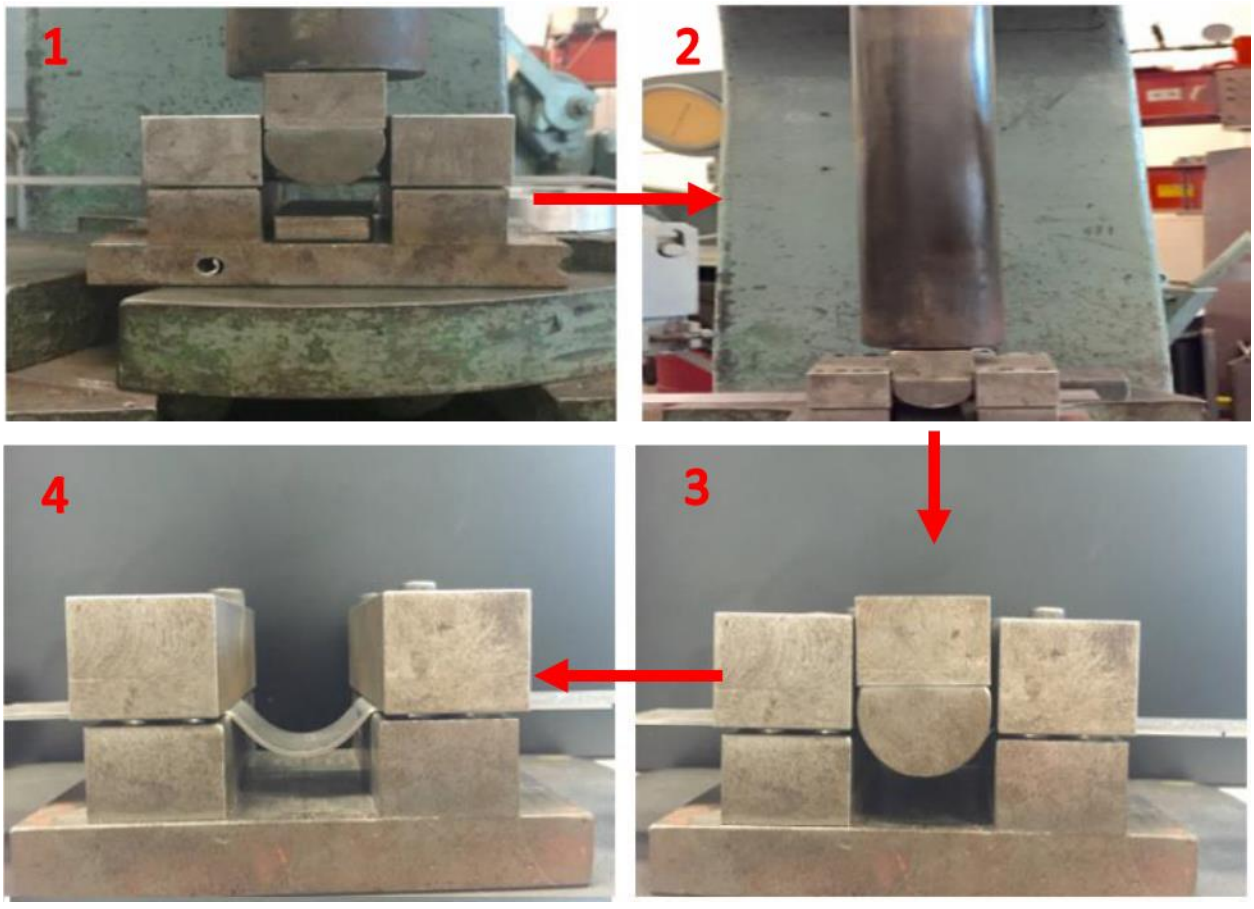

Figure 2.5 Stamping process (clockwise from top left)

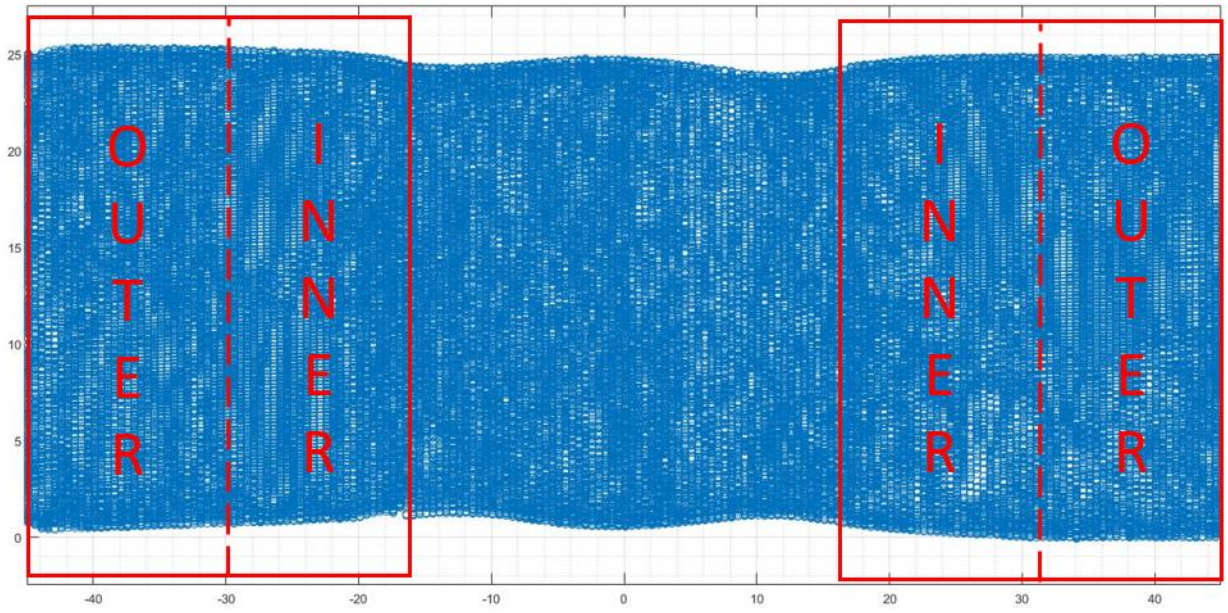

Figure 2.6 Variation in beam width at the dimple and in clamped locations

It is important to note that the beams examined here were initially used by previous researchers [5], [7]. Using the same beams provides a common basis for comparing results from this study to those presented in previous work.

An important admission to make here would be that this author has not made any dimpled beams. The reason for that lies in the objective of this research being investigating the effect of stamping on the vibrational performance of dimpled beams rather than studying new beams. Consequently, the plan of action is arriving at results generated by previous authors using a different technique and assessing the dissimilarities observed. If this author had made new dimpled beams, there would be no benchmark with which to compare the findings.

2.3. Summary

Although the setup is simple and easy to operate, it has a couple of drawbacks. The first one is its uncontrolled nature. Since there is no way to measure the distance the press (and the plunger in turn) travels down, a reasonable degree of control cannot be exercised over the dimple height and consequently angle. Another shortcoming is the fixed distance between the two sets of clamping blocks. This necessitates the use of a plunger with a diameter that matches this dimension. While it can be argued that a plunger of any size can be used as long as it fits in that

gap, the fixed distance between the clamping blocks will allow the beam to deform along that whole length and the resulting dimple will not have the size and shape of the plunger as intended.

3. Tension testing

Stamping creates considerable plastic strains in the beam. Prediction of this deformation requires that the stress-strain behavior of the beam material be known so that it can be used as an input to the simulation to be presented. This stress-strain behavior of the material, in addition to its Young's modulus (modulus of elasticity) and yield strength, can be determined using a uniaxial tension test.

This chapter describes the uniaxial tension test performed on a sample of the beam material according to the relevant ASTM standard [10]. The manufacturing of the test specimen is explained in Section 3.1, while the test procedure is covered in Section 3.2. Material properties are computed from the test data in Section 3.3 and Section 3.4 provides a brief summary.

3.1. Manufacturing the test specimen

The standard provides instructions for tension testing for a variety of specimen shapes (flat, round, tubular etc.) and manufacturing methods (machining, casting, powder metallurgy etc.) along with guidelines for selecting the appropriate one. Irrespective of its cross-section, a tension testing specimen usually consists of broad ends for gripping and a reduced section in the middle to facilitate failure. The shape and dimensions of the test specimen are shown in Figure 3.1 *Shape and dimensions of the tension testing specimen*

Figure 3.2 Process for machining the test specimen (clockwise from top left)Figure 3.1. Interested readers are advised to refer to the ASTM standard for a more detailed sketch.

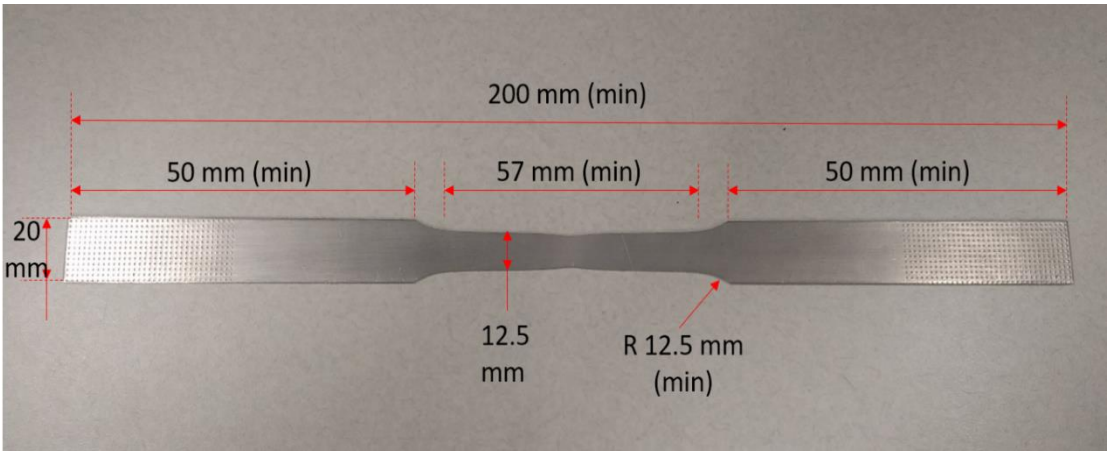

Figure 3.1 Shape and dimensions of the tension testing specimen

The standard's guidelines for testing sheets, strips, flat wires and plates with thickness of 0.13 mm to 5 mm were followed and a 12.5 mm wide sheet-type specimen was chosen. A CNC machine was used to machine a strip of the beam material to the standard's specifications. Clamps were used to hold the strip down on a fixture, while the reduced width portion was machined on the side opposite to the clamps. Then, the clamps were transferred to the machined side of the specimen, while the previously clamped side was machined. This process is illustrated in Figure 3.2 *Process for machining the test specimen (clockwise from top left)*.

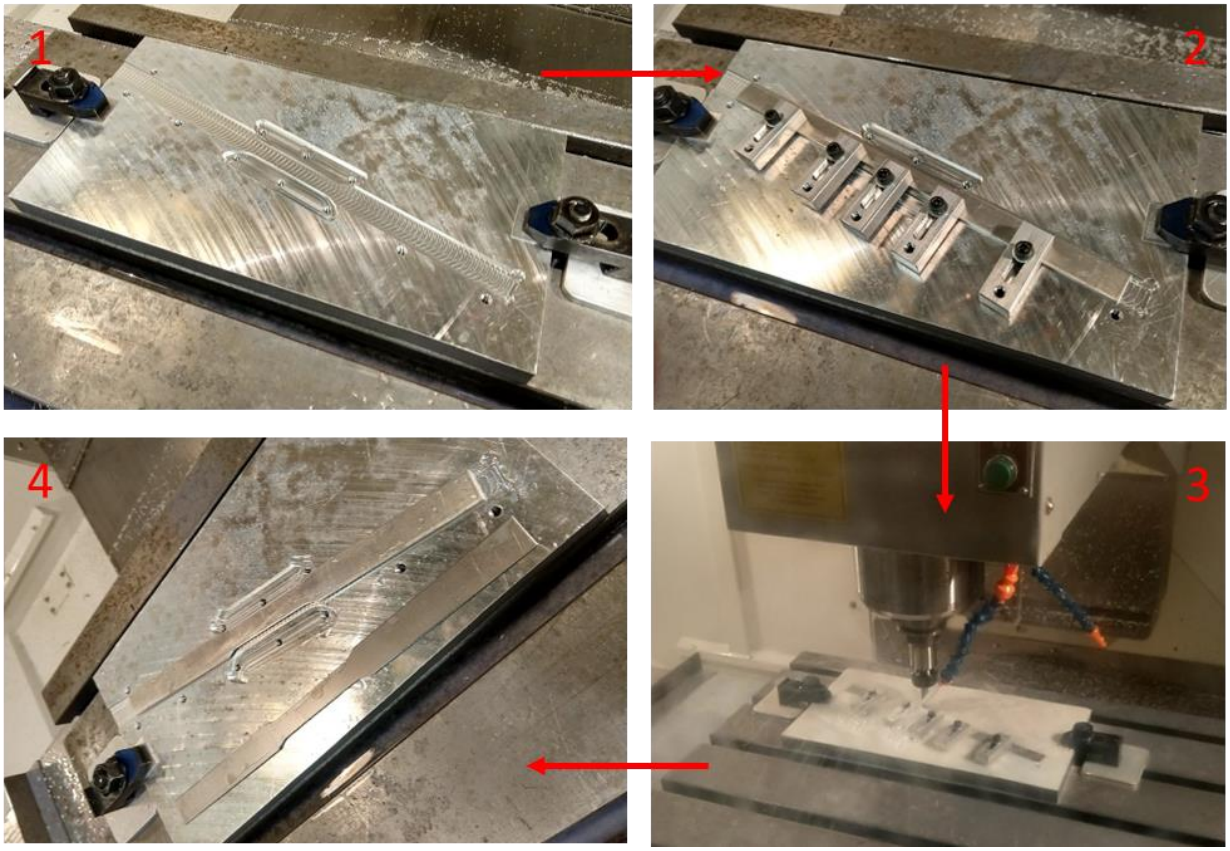

Figure 3.4 Process for machining the test specimen (clockwise from top left)

3.2. Performing the uniaxial tension test

With the specimen machined and ready, the uniaxial tension test is carried out using the MTS 810 Material Test System shown in Figure 3.3 *The MTS 810 Material Test System used to perform the uniaxial tension test*. The specimen, with an attached extensometer measuring axial strain, is firmly clamped between the jaws of the machine (Figure 3.4 *Front view (left) and side view (right) of test specimen clamped in the jaws of the machine with the attached extensometer visible as well*). The jaws apply tensile force by slowly pulling the specimen apart at a set rate, while also recording the force and displacement in the axial direction. This tensioning of the specimen is continued until the failure of the material occurs as shown in Figure 3.5 *Test specimen after failure*

Figure 3.6 Stress-strain curve of beam material obtained from uniaxial tension testFigure 3.5.

Figure 3.5 The MTS 810 Material Test System used to perform the uniaxial tension test

Figure 3.6 Front view (left) and side view (right) of test specimen clamped in the jaws of the machine with the attached extensometer visible as well

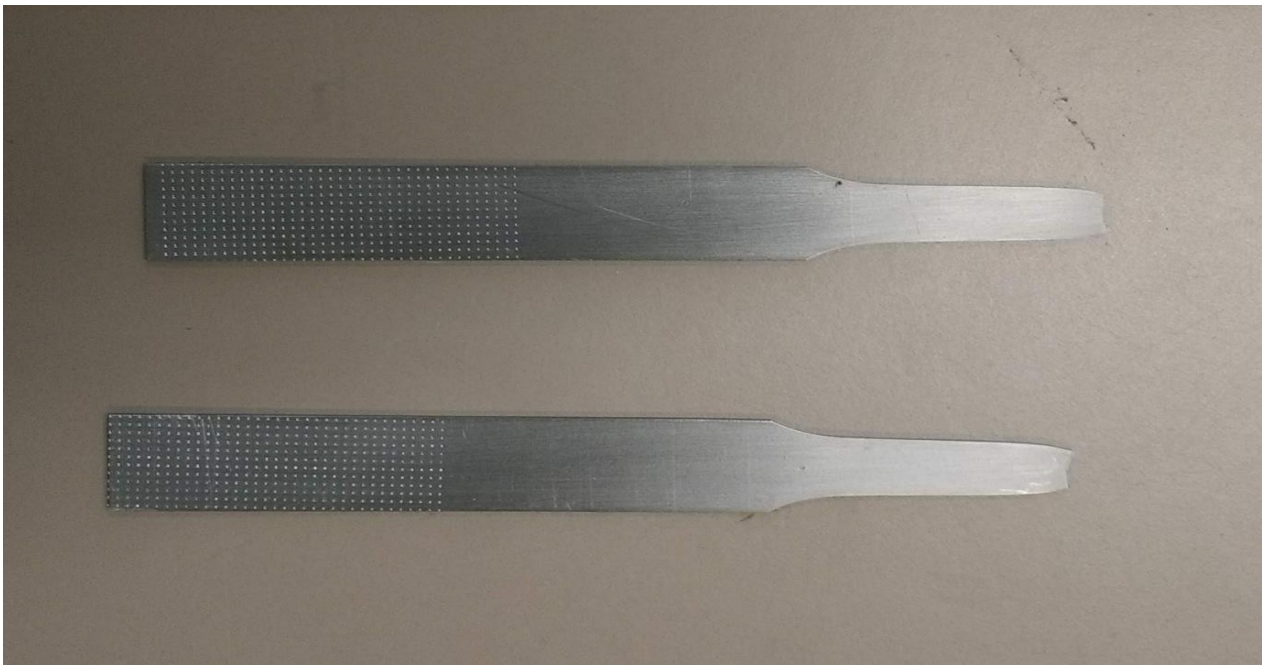

Figure 3.7 Test specimen after failure

3.3. Calculation of material properties from test data

Values of stress are obtained by dividing the measurements of force by the initial cross-sectional area of the specimen. Two details are of importance here. Firstly, the cross-sectional area is calculated for the reduced width portion of the specimen, since that is where the failure occurs. Secondly, dividing the force by the initial cross-sectional area gives engineering values of stress and not the true stress [11, p. 44]. Plotting these values of stress and strain create a picture of the material behavior over its entire range of strain, which can then be used as an input to the FE model. Figure 3.6 *Stress-strain curve of beam material obtained from uniaxial tension test* shows this stress-strain curve. It displays a linear stress-strain relationship in the elastic region, followed by yielding and a continuous increase in stress and strain till the point of maximum stress is reached. Thereafter, although the strain continues to increase, a decline in stress is observed and the specimen eventually fails.

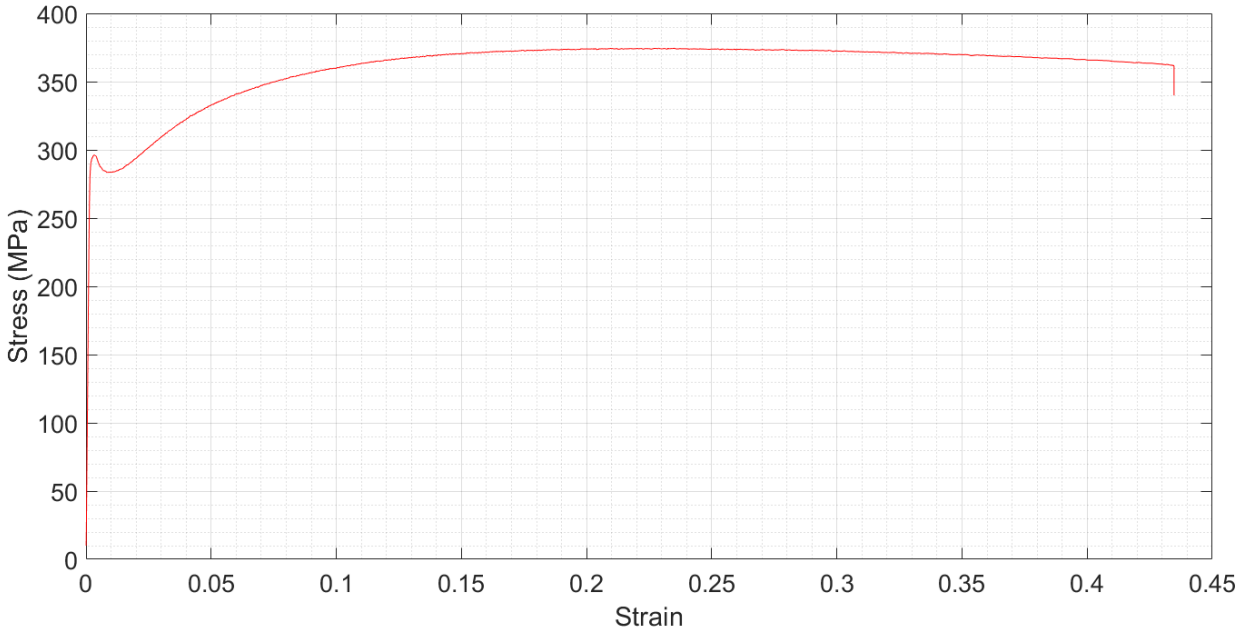

Figure 3.10 Stress-strain curve of beam material obtained from uniaxial tension test

Young's modulus can also be derived from this stress-strain data by fitting a straight line to all the points in the linear portion of the curve found in the elastic region. The slope of this line is the Young's modulus of the beam material, which comes out to 196 GPa. For comparison, Alshabtat [5, p. 91] and Ghazwani [7, pp. 56,62] used values of 190 GPa and 200 GPa respectively.

It must be noted that they obtained these values from literature and not from tension testing of the beam material.

3.4. Summary

A uniaxial tension test was carried out in accordance with ASTM standard E8/E8M – 16a for Standard Test Methods for Tension Testing of Metallic Materials to evaluate the stress-strain behavior and other mechanical properties of the beam material. A 12.5 mm wide sheet-type specimen was machined according to the standard's specifications and used for testing in an MTS 810 Material Test System. Measurements of force, displacement and strain in the axial direction were obtained from this test. Values of force from this data were then divided by the initial cross-sectional area of the reduced width portion of the specimen to convert them to stress. This data was used to calculate the Young's modulus and yield strength of the material.

4. Finite Element simulation of the stamping process

As mentioned in Chapter 2, the dimples are manufactured using stamping. A finite element (FE) simulation of this process is performed using Mechanical ANSYS Parametric Design Language (APDL or MAPDL) module in ANSYS 19.1. This approach allows the parameterization of almost every aspect of the simulation and hence, lends itself to observing the effects of changes in certain parameters on the end results.

Section 4.1 describes the basics of creating a 3-D parametric model and the initial setup, while Sections 4.2 and 4.3 describe the nonlinearities in the simulation and material properties used respectively. Section 4.4 illustrates the meshing of the model and Section 4.5 details the contact setup. Finally, Section 4.6 expounds on the boundary conditions implemented and the solution phase of the FE model with Section 4.7 providing the summary.

4.1. Creating a 3-D parametric model and initial setup

The stamping setup described earlier is not recreated in its entirety for the finite element model. Only the flat strip of metal (hereafter referred to as beam) and the plunger are physically modelled as shown in Figure 4.1 *Finite element model of beam and plunger (unmeshed). Images used courtesy of ANSYS, Inc.*, while the effects of the clamping blocks are modelled by appropriate boundary conditions. Several important variables such as the beam dimensions, dimple location, element size and displacement of the plunger are represented by parameters.

4.2. Nonlinearities in the simulation

As mentioned before, the beam deformation resulting from the stamping process is permanent and falls within the plastic region. Thus, any modeling of this process must consider plastic deformation and the inherent nonlinearities of material and geometry.

The presence of nonlinearities usually means the FE software performs an iterative solution and updates the stiffness matrix after every iteration to account for the changes in nodal displacements. A structural finite element analysis (FEA) usually deals with three kinds of nonlinearities: material nonlinearities, geometric nonlinearities and contact nonlinearities.

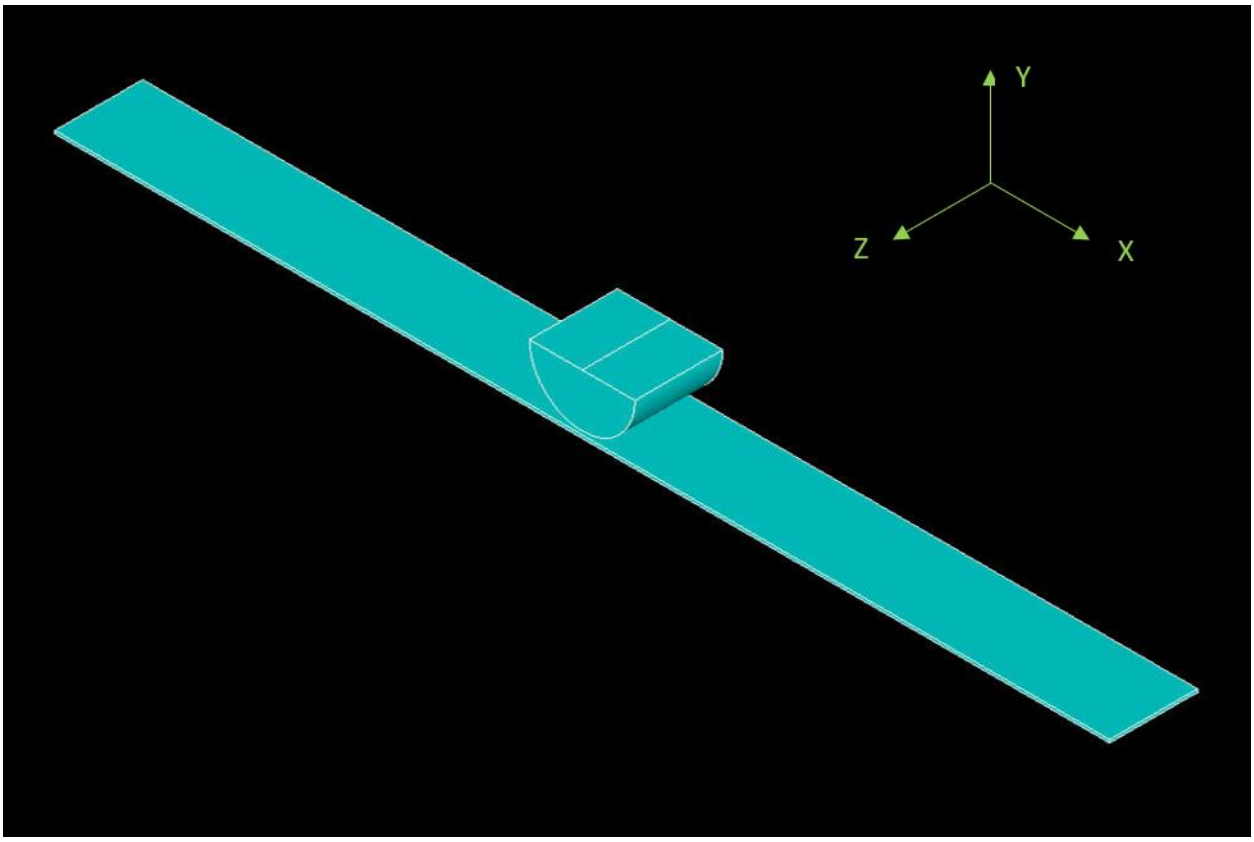

Figure 4.1 Finite element model of beam and plunger (unmeshed). Images used courtesy of ANSYS, Inc.

4.2.1. Material nonlinearities

The stress-strain behavior of metals, such as steels, is typically described by a curve showing a proportional relationship to a point signifying reversible elastic deformation followed by a nonlinear portion leading to the point of maximum stress and eventual failure. Material nonlinearities pertain to this nonlinear part of the curve past the elastic limit as it is characterized by phenomena such as yielding and strain hardening. A variety of material models are available to describe this behavior and choosing the model that best fits the application is often critical to achieving results with physicality [12]. Here, plastic deformation is described by a nonlinear model with rate-independent plasticity.

The only other significant effect that the material model needs to capture is strain hardening. There are two hardening rules available to model this: kinematic and isotropic [13, pp. 384-388]. The choice of the hardening rule is governed by the kind of loading involved.

Kinematic hardening can capture the effects of cyclic loading well since it can model the Bauschinger effect where the compressive yield strength reduces in response to tensile yielding [14, p. 95]. Isotropic hardening, on the other hand, is better suited to model behavior of materials under monotonic loading and elastic unloading [12, p. 134]. As the loading involved in stamping is of the latter type, isotropic hardening is chosen to capture the effect of strain hardening. Mathematical formulations of these hardening rules and their implementation in nonlinear FEA can be found in [13, pp. 367-391].

After the choice of hardening rule is made, it must be decided whether bilinear hardening or multilinear hardening will be used. As shown in Figure 4.2 *Bilinear (left) and multilinear (right) hardening models*, this decision affects the material behavior in the plastic region. As is evident from their names, bilinear hardening condenses the stress-strain behavior into two straight lines. The first line extends to the elastic limit and a second straight line directs the behavior in the plastic region. The slope of the first line equals the elastic modulus and that of the second line is equal to what is known as the tangent modulus. This tangent modulus is not a measurable property and instead is often assumed to be a certain percentage of the elastic modulus. There are no standard rules for selecting this percentage value and recommendations range from 0.1% to 10%. In multilinear hardening, the first line covers the region till the elastic limit, but the nonlinear portion of the stress-strain curve is approximated by a series of line segments plot using data from a uniaxial tension test. Multilinear hardening is the more accurate of the two and is used herein.

The data from the tension test cannot be used for the simulation without some post-processing. Sometimes, substantial distortion of individual elements produces local stresses and/or strains exceeding the maximum values of engineering stress-strain for the material. However, this carries no physical relevance and it is advisable to avoid such a situation by using a blend of the bilinear and multilinear hardening rules in the input stress-strain curve. Figure 4.3 *Sample stress-strain data used as input to ANSYS and data from tension test* is the result of this pragmatic post-processing.

Looking at the multilinear hardening curve shows that each successive segment becomes flatter after the elastic limit i.e. the slope goes from close to the elastic modulus to near zero at ultimate stress. Once they start to flatten out, a segment whose slope comes closest to the 'tangent modulus' is picked and data up to this point is selected. One last line segment with a slope equal to the tangent modulus is then grafted to end of this curve and its end point is set considerably higher than the ultimate stress, purely for ease of implementation.

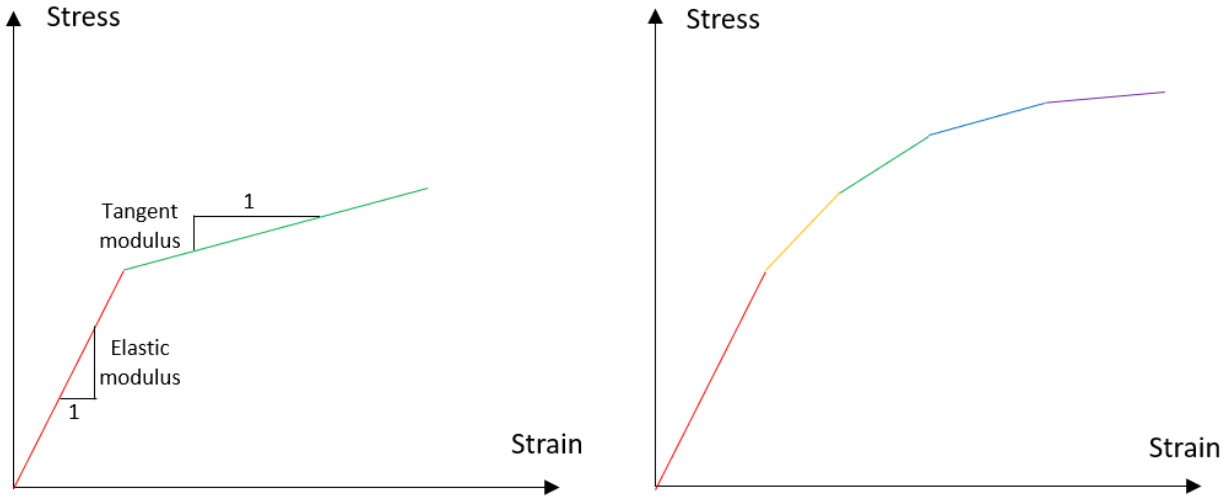

Figure 4.2 Bilinear (left) and multilinear (right) hardening models

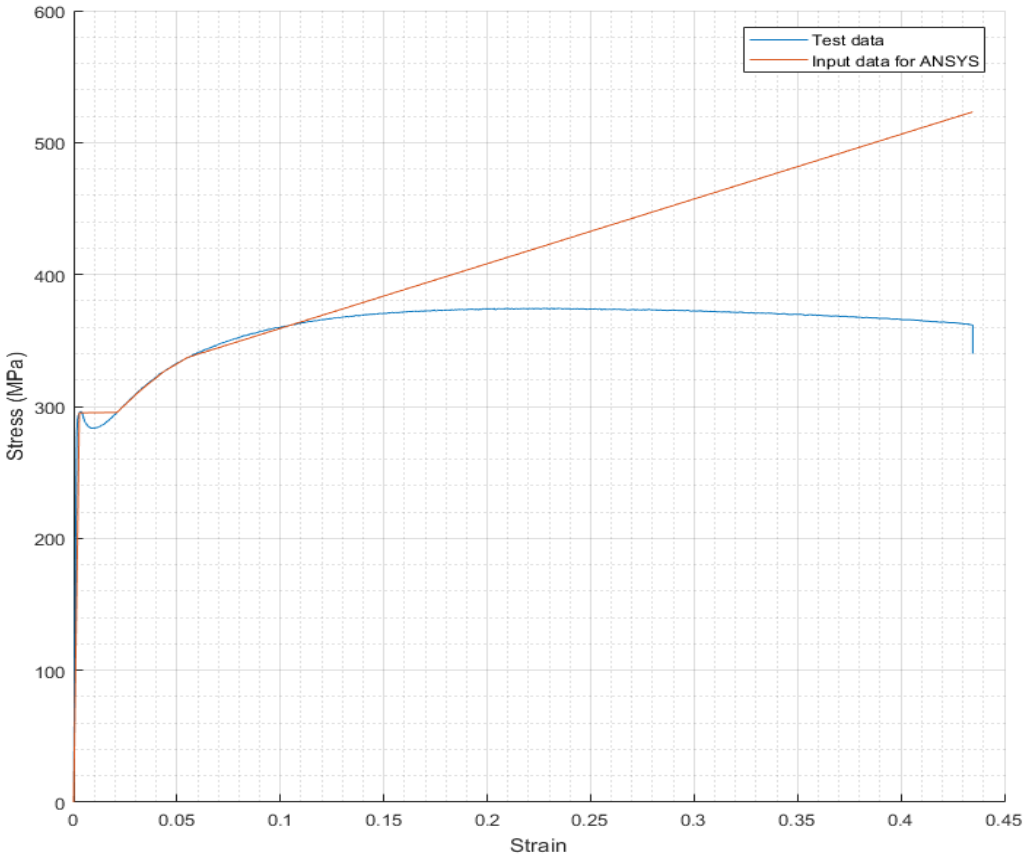

Figure 4.3 Sample stress-strain data used as input to ANSYS and data from tension test

There is one more adjustment that needs to be made due to software limitations. ANSYS does not allow negative slopes in the stress-strain data entered, which is exactly what is seen in the test data. When the material yields, there is a dip in stress before it continues its upward trend. The strain, however, keeps increasing and this results in negative slope. There are two methods to overcome this, as shown in Figure 4.4 *Negative slope avoidance method 1*

Figure 4.5 Negative slope avoidance method 2Figure 4.4 and Figure 4.5 *Negative slope avoidance method 2*

Figure 4.6 Finite element model of beam and plunger after meshing. Images used courtesy of ANSYS, Inc.Figure 4.5. Method 1 involves picking the upper yield point and a second point after

the dip such that the slope of the line segment connecting the two is slightly greater than zero. In method 2, the part of the curve after the lower yield point is extended back till it intersects the straight line in the elastic region of the curve.

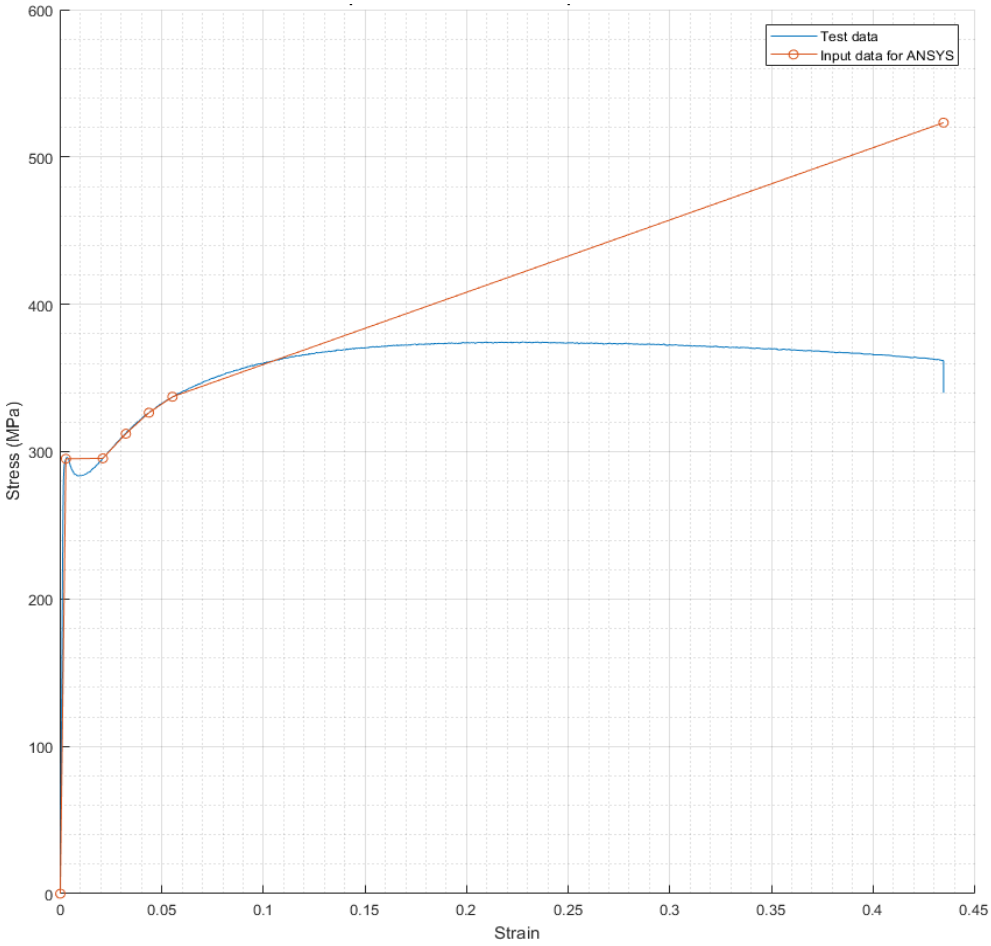

Figure 4.4 Negative slope avoidance method 1

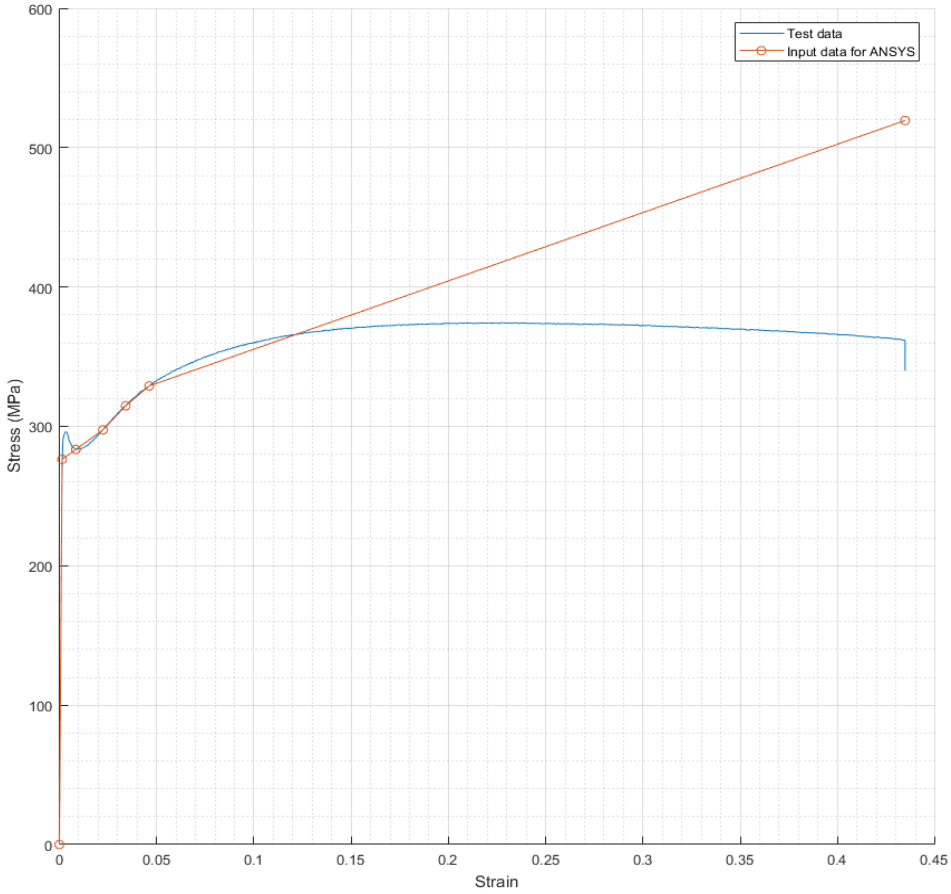

Figure 4.7 Negative slope avoidance method 2

It is worth examining the effects of using each of these methods on the material behavior and their physical implications. The area under the stress-strain curve denotes the amount of energy that the test specimen absorbs before failure. In method 1, the dip in stress after yielding is ignored and replaced by a straight line with a small positive slope. This increases the area under the curve slightly, meaning the material in the simulation absorbs more energy than it does in reality. Also, the small positive slope of the straight line translates to a very low resistance to deformation. Method 2, on the other hand, eliminates the upper yield point and thereby implies that the material absorbs less energy. This also means that the material yields at a lower value of stress as compared to the test specimen. The implementation of both these methods affects the deformation of the beam during stamping and that, in turn, influences its vibrational behavior. These effects are investigated by producing vibrational results using both approaches and comparing them to their experimental counterparts (See Section 8.2).

4.2.2. Geometric nonlinearities

Geometric nonlinearities involve large deflections/rotations and large strain. Large deflections/rotations might be results of significant strains or simply rigid body movement of the structure. It is advisable to consider this when the final geometry of the structure is markedly different than its initial state. Large strains refer to strains in magnitude beyond the ones encountered at the material's elastic limit and causing irreversible plastic deformation. The existence of large strains in the simulation inexorably leads to the use of a nonlinear material model. The FEA considers both large deflections/rotations and large strains since they are expected from creating a dimple.

4.2.3. Contact nonlinearities

As mentioned at the beginning of this section, nonlinearities force the FE software to perform an iterative solution and update the stiffness matrix with every iteration. Friction though contact between the plunger and the beam is responsible for the transfer of forces between them. This transfer directly causes significant changes to the beam geometry and consequently, its stiffness, meaning nonlinearities are introduced due to the contact. Here, a coefficient of friction is used to account for this effect. Nevertheless, friction is a highly unpredictable and complex phenomenon especially in the present scenario. Therefore, while the use of a coefficient of friction mostly captures its impact, there is bound to be a small measure of uncertainty and discrepancy between the simulation and the experimental results.

4.3. Assigning nonlinear material properties

The stamping process is simulated using a nonlinear static structural analysis, which requires the input of several key material properties such as the modulus of elasticity, Poisson's ratio, the coefficient of friction between the plunger and the beam and finally, the density and stress-strain behavior of the beam material. As per Section 4.2.1, the stress-strain properties and modulus of elasticity are obtained from the tension test, while values for Poisson's ratio, density [15] and coefficient of friction [16, pp. 2-44] are obtained from material data sheets. It must be noted that the value of coefficient of friction used is for sliding friction between dry surfaces since there is relative motion between the plunger and the beam during dimple creation. All these properties are summarized in Table 4.1.

.

Table 4.1 Material properties of beam

Property	Value used
Modulus of elasticity	196 GPa
Poisson's ratio	0.29
Coefficient of friction	0.52
Density	7870 kg/m^3

4.4. Meshing the model

As the model is three-dimensional, solid elements are used to mesh it. Two different kinds of elements are used for the plunger and the beam. The plunger is meshed using SOLID187 elements, while SOLID186 elements are used for the beam. Both are 3-D solid elements with three degrees of freedom at each node, namely translations in the X, Y and Z directions. Also, some of their capabilities include plasticity, stress stiffening, large deflection and large strain. SOLID186 has 20 nodes and by default, is in the shape of a rectangular cuboid, while SOLID187 has 10 nodes with its default shape being a tetrahedron [17].

The reasoning for choosing SOLID186 for the beam and SOLID187 for the plunger is rooted in practical considerations. The primary objective here is accurately simulating the deformation of the beam and consequently, it makes more sense to devote a greater share of computational resources to the meshing of the beam. Since the beam is subjected to large deflections and strain and undergoes extensive deformation, its mesh tends to get distorted. Hence, to avoid severe distortions, it is advisable to avoid large aspect ratios for its elements when it is initially meshed. SOLID186 completely fulfills this condition since it can be meshed as cubes in a relatively fine mesh. On the other hand, this shape does not lend itself very well to the curved geometry of the plunger. Also, the plunger's deformation is not of interest to us and it does not make sense to mesh it with an element having 20 nodes. SOLID187 with its tetrahedral shape and 10 nodes per

element is thus more useful for meshing the plunger. Figure 4.6 *Finite element model of beam and plunger after meshing. Images used courtesy of ANSYS, Inc.*

Figure 4.7 Contact surfaces with outward normals shown in blue. Images used courtesy of ANSYS, Inc.Figure 4.6 shows the meshed model with the differences in the fineness of mesh on the beam and the plunger clearly visible.

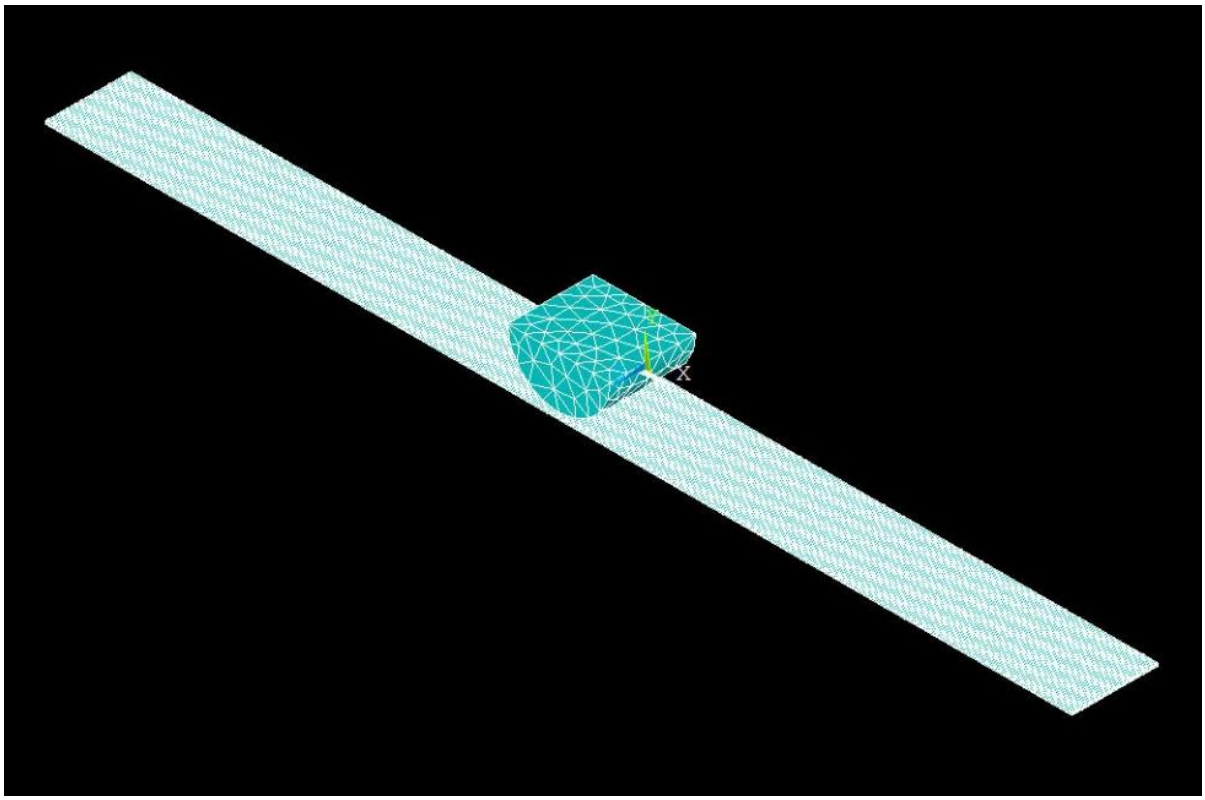

Figure 4.10 Finite element model of beam and plunger after meshing. Images used courtesy of ANSYS, Inc.

4.5. Setting up contact

Setting up contact between the plunger and the beam is a critical part of the simulation. All the simulation must accomplish is to make the plunger come down on the clamped beam and deform a part of it into the dimple. However, this is not possible without contact elements as without them, the plunger will simply pass through the beam without ever deforming it. The presence of contact elements on the surfaces of the beam and the plunger is the mechanism for their interaction. Also, after the plunger has completed its downward motion and moves back

up, the dimple undergoes some elastic recovery, which is also facilitated by the contact elements. Thus, the accuracy of the deformed shape of the beam depends, to a large extent, on contact being modelled right.

The first step is identifying the surfaces coming into contact and designating them as such. Here, that would be the curved surface of the plunger and the surface of the beam that it touches. Together, they form what is known as a contact pair. Secondly, elements used to specify contact fall into two main categories, namely target elements and contact elements. Although there are no set rules, general guidelines are available to help decide what kind of elements will be generated on which surface of the contact pair. The deciding factors relevant here are the fineness of the mesh and rigidity that each surface is required to exhibit. The surface with the coarser mesh should be designated as the target surface, which makes the surface with the finer mesh, the contact surface. Also, in the case of rigid to flexible contact, the rigid surface should be the target surface and the deformable surface should be the contact surface. In this case, the plunger's mesh is coarse, and it must be rigid. Consequently, it is designated as the target surface. It follows that it is populated with target elements while contact elements are generated on the beam's surface.

The next step is selecting the specific element of that kind. The choices available for contact elements (beam's surface) are CONTA173 or CONTA174. While both these elements have similar contact technologies available to them, the selection is dependent on the kind of underlying elements. As higher order SOLID186 elements were used to mesh the beam, CONTA174 are chosen for the beam. On the other hand, the only element choice available for the plunger is TARGE170 and is used accordingly.

A couple of other important points are the KEYOPT settings and directions of the outward normals. KEYOPT settings allow close control of the contact behavior. Besides regular displacement degrees of freedom (DOFs), CONTA174 elements have several other DOF options like voltage and temperature available. As those are irrelevant, translations in the X, Y and Z directions are selected as the only valid DOFs. For TARGE170 elements, boundary conditions are specified as user-defined as opposed to program-controlled. This allows friction to be

incorporated into the simulation and takes it closer to reality since no lubrication was used between the plunger and the beam. As for the directions of the outward normals, the normals from the contact surface must point to the target surface and vice versa. Usually, this condition is automatically fulfilled as the direction of the outward normal from a contact element coincides with the direction of the outward normal from the underlying solid element. Figure 4.7 *Contact surfaces with outward normals shown in blue. Images used courtesy of ANSYS, Inc.* shows the model with the outward normals in the correct orientation.

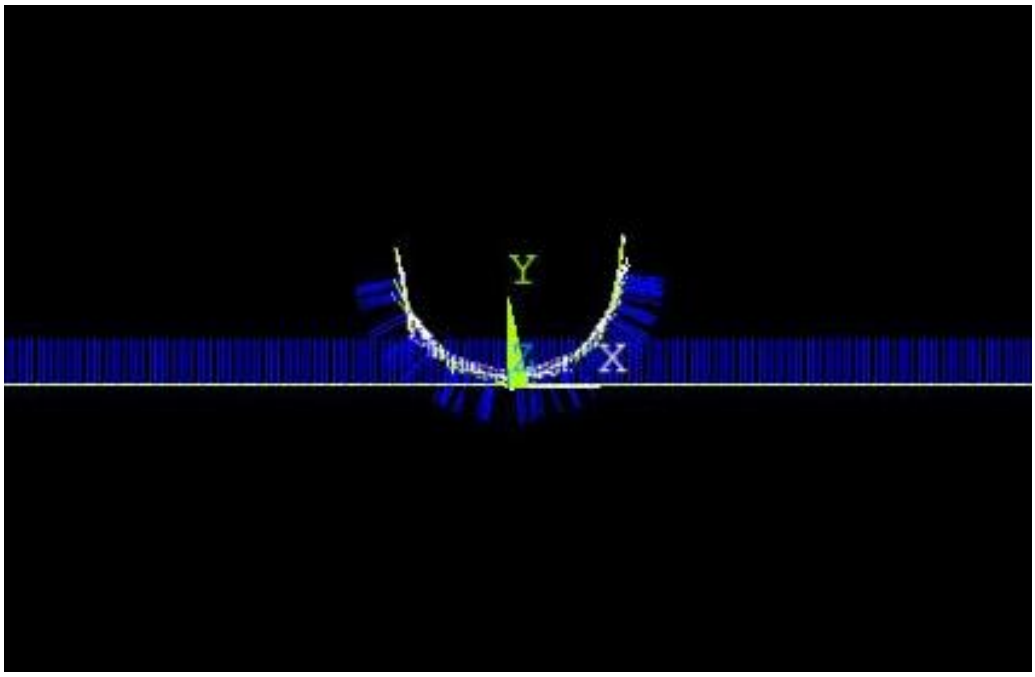

Figure 4.13 Contact surfaces with outward normals shown in blue. Images used courtesy of ANSYS, Inc.

The outward normals denote the direction of the transfer of force and displacement from the plunger to the beam. It is worth remembering here that both these bodies are meshed with different degrees of fineness. While that is a necessary measure for accommodating the model within the computational constraints, it has an unintended side effect. The differing degrees of mesh fineness are likely to cause a mismatch of nodes along the contact surfaces. This in turn can cause transfer of forces from the plunger to the beam along directions that are not perpendicular to the beam's surface.

4.6. Boundary conditions and solution

Now that the modelling and meshing is finished, specifying the boundary conditions is all that remains. This is a two-step process. The first step is recreating the effects of the clamping blocks as mentioned in Section 4.1, while the second one is defining the descent and subsequent return of the plunger.

As illustrated in Figure 2.4 *Variation in beam width at the dimple and in clamped locations* of Section 2.2, the constraints imposed by the clamping blocks on the beam are slightly unusual in that their behavior changes halfway through. Proceeding from the dimple to the clamped portion of the beam, it is observed that the beam width narrows halfway through i.e. the clamps allow deformation along the width in the inside half of the beam, while no deformation is allowed in the outside half of the clamped portion of the beam. Since the width changes in the inner half, it follows that deformation is also permitted along either the thickness or length dimensions to allow for the lateral strain as dictated by Poisson's ratio and material plastic flow. However, Figure 4.1 *Finite element model of beam and plunger (unmeshed). Images used courtesy of ANSYS, Inc.* shows that the plunger travels in the Y direction, which is along the thickness, and the whole point of the clamps is to prevent any movement in that direction. Thus, it is evident that clamps allow deformation in the length (X) and width (Z) directions, while constraining the beam along the thickness (Y) direction. The constraining behavior is straightforward in the outer half in that deformation is prevented in all three directions. This complexity is encapsulated in the FE model by selecting the appropriate beam nodes and constraining them in a manner similar to what is observed.

With the effects of the stamping setup approximated, the boundary conditions to simulate the stamping process itself can now be specified. As the first step, the plunger closes the initial gap between itself and the beam by travelling a distance equal to 90% of this gap. This is then saved as the first load step. As the next steps of the simulation involve plastic deformation and material nonlinearities, it is best carried out at a slow pace to avoid convergence difficulties and maintain the 'static' nature of the FEA. So, the displacement of the plunger from this point onwards is specified in increments of 0.1 mm each. This increment is very small compared to the total distance of 11.5 mm that the plunger travels to create a 135° dimple. It travels downward

for a distance calculated by the dimple height equation shown in Section 2.1 and then goes back up for a quarter of that distance to allow elastic recovery of the dimple. Additionally, as many as 500 sub-steps may be used to facilitate convergence. Finally, all these steps are used as sequential inputs to the solver in order to simulate stamping. Figure 4.8 *Steps in the FE simulation of stamping (clockwise from top left). Images used courtesy of ANSYS, Inc.* shows an abbreviated sequence of the creation of a single dimple in the center of a beam.

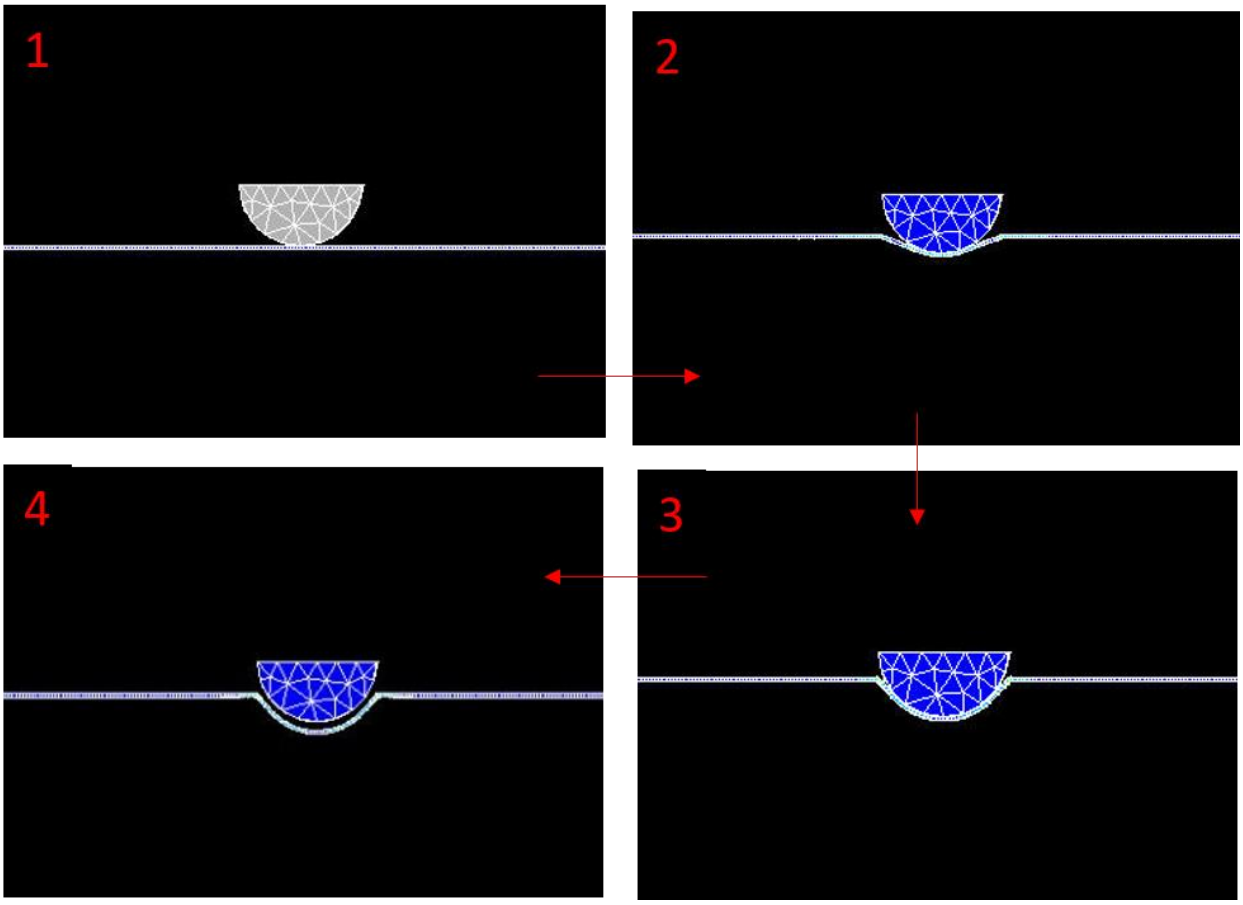

Figure 4.14 Steps in the FE simulation of stamping (clockwise from top left). Images used courtesy of ANSYS, Inc.

4.7. Summary

The FE simulation of the stamping process was accomplished by creating a 3-D parametric model, assessing the nonlinearities present in the physical process and including their effects in the FEA. Based on tension testing, the beam material was approximated as an isotropic material with a mix of bilinear and multilinear hardening behavior. The system was modelled, meshed,

and suitable contact behavior was set up between the plunger and the beam. The effects of the clamping blocks from the stamping fixture were approximated by implementing suitable boundary conditions and the software was instructed on the manner of conducting the analysis. It must be noted that the procedure to simulate the creation of two dimples was practically the same. Two plungers were modelled, and they created dimples one at a time.

5. Validation of finite element model of stamping

Chapter 4 detailed modeling of the process of stamping using finite element (FE) software. This chapter describes the validation of that model by comparing the thickness and width of the FE beam to measurements made on its real-life counterpart. Section 5.1 illustrates the procedure followed for measurements of width and thickness of the physical beam while Section 5.2 explains the calculation of width of the FE beam and its comparison with the measurements. Section 5.3 follows suit by expounding on the relatively complex process of calculating the thickness of the FE beam and comparing it with the respective measurements. Finally, Section 5.4 provides explanations for the differences observed in previous comparisons and Section 5.5 concludes the chapter.

5.1. Measurement of beam thickness and width

The thickness of the beam is in the one-millimeter range, so a DBM Imports micrometer was used to measure it and the beam's width was measured by a TTC make digital caliper. Figure 5.1 *Point micrometer (Range: 0-1" and least count 0.0001")*

Figure 5.2 Digital caliper (Range 0-150 mm and least count 0.01 mm)Figure 5.1 and Figure 5.2 *Digital caliper (Range 0-150 mm and least count 0.01 mm)* show both these instruments, while Figure 5.3 *Measurement of beam thickness using a point micrometer* and Figure 5.4 *Measurement of beam width using a digital caliper*

Figure 5.5 Paper tape on the beam acting as a measuring scale and centerline markerFigure 5.4 show them in use. It was noted earlier that the thickness varies along the length of dimple and areas in its immediate vicinity. Given the mechanics of beam deformation, the likelihood of variations in the beam thickness along its width cannot be ruled out. In that case, if a regular micrometer (having flat ends) was used, it would measure only the highest thickness encountered over the surface of its flat end. Hence, a point micrometer was used to measure the thickness accurately at the point of contact. As shown in Figure 5.5 *Paper tape on the beam acting*

as a measuring scale and centerline marker, paper tape was applied to the surface to the beam to serve the dual purpose of being a measuring scale and marking the location of the beam's centerline. Thus, the thickness was measured at 5 mm intervals along the centerline of the beam. Thickness and width of the flat undeformed portions of the beam were found to be 0.844 mm and 25 mm respectively.

Figure 5.1 Point micrometer (Range: 0-1" and least count 0.0001")

Figure 5.4 Digital caliper (Range 0-150 mm and least count 0.01 mm)

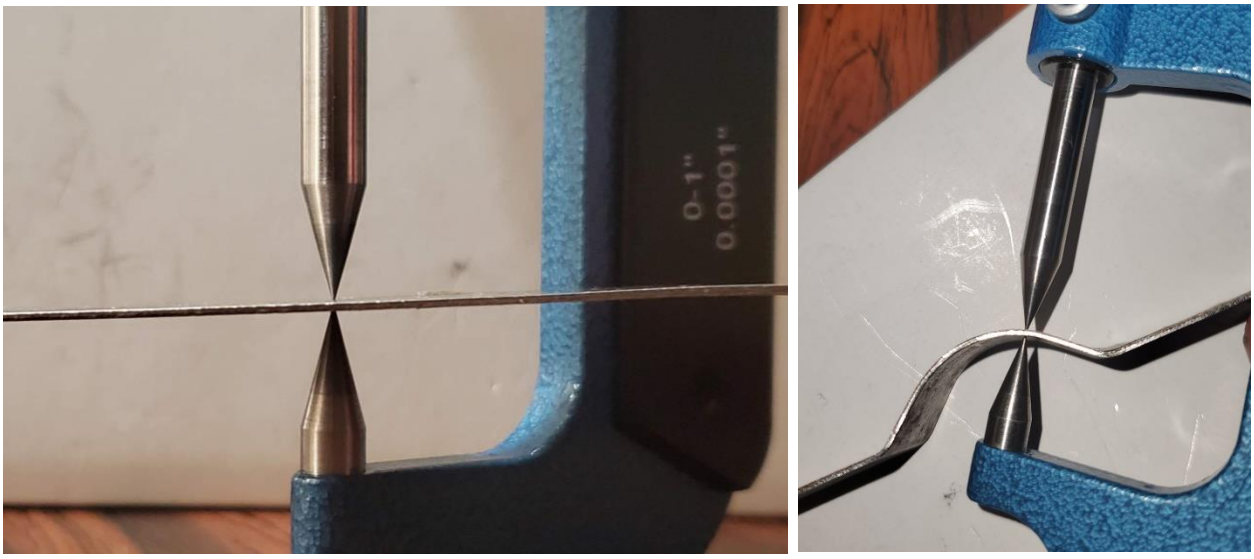

Figure 5.5 Measurement of beam thickness using a point micrometer

Figure 5.6 Measurement of beam width using a digital caliper

Figure 5.9 Paper tape on the beam acting as a measuring scale and centerline marker

5.2. Calculation of width of FE beam and comparison with measurements

As explained in Chapter 4, a static structural finite element analysis (FEA) is carried out to simulate the process of stamping and create a dimple on a beam. After the simulation is complete, a list of all the nodes on the beam, along with their unique node numbers and coordinates, is saved. The data in this list is imported into MATLAB for further processing and used to calculate the thickness and width of the FE beam.

To calculate the beam's width, points at either edge of the beam along its Z direction are selected (refer to Figure 4.1 *Finite element model of beam and plunger (unmeshed). Images used courtesy of ANSYS, Inc.* for the orientation of coordinate axes). As both points have the same X and Y coordinates, the difference between their Z coordinates is the beam width. Figure 5.6 *Points selected from the FE model to calculate beam width*

Figure 5.7 Comparison of width calculated from FEA to its measured valuesFigure 5.6 shows such a selection of points centered on the area of the dimple. Figure 5.7 *Comparison of width calculated from FEA to its measured values* shows the comparison of these calculations of

width to the measurements made using digital calipers along with % error in Figure 5.8 *Comparison of calculated and measured width with % error*. Clearly, both sets of data follow the same symmetrical trends i.e. a reduction in width at the start of the dimple followed by a region of recovery culminating in maximum width at the dimple center. Having said that, it can also be observed that the magnitude of peaks and valleys in the FEA data are different than in the measured data. In the FEA data, the dip at the beginning of the dimple goes deeper, while at its center, it manages to recover to almost its full width. On the other hand, the reduction in the measured width at the beginning of the dimple is less severe and even after the recovery at the dimple center, the width still stays considerably below what is measured at the flat portion of the beam. These trends will be elaborated on in Section 5.4.

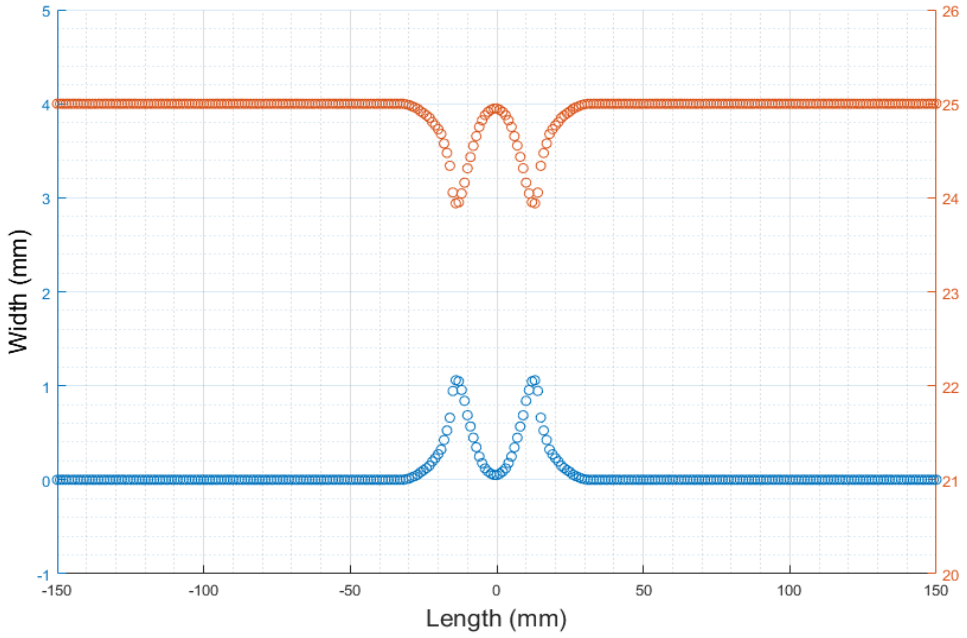

Figure 5.10 Points selected from the FE model to calculate beam width

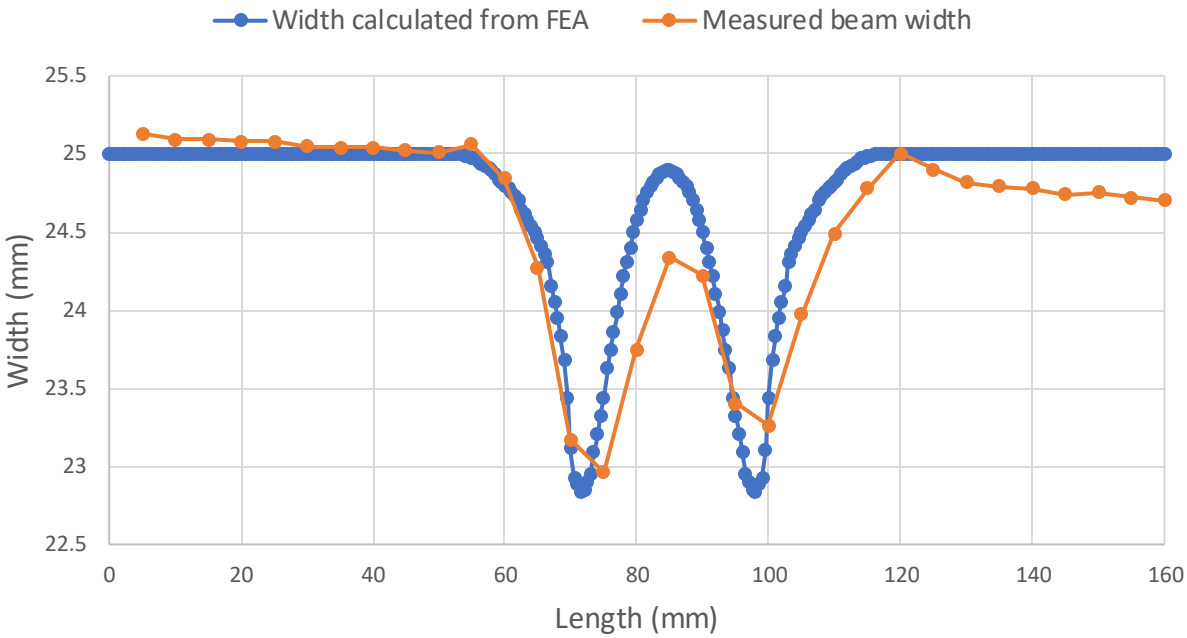

Figure 5.13 Comparison of width calculated from FEA to its measured values

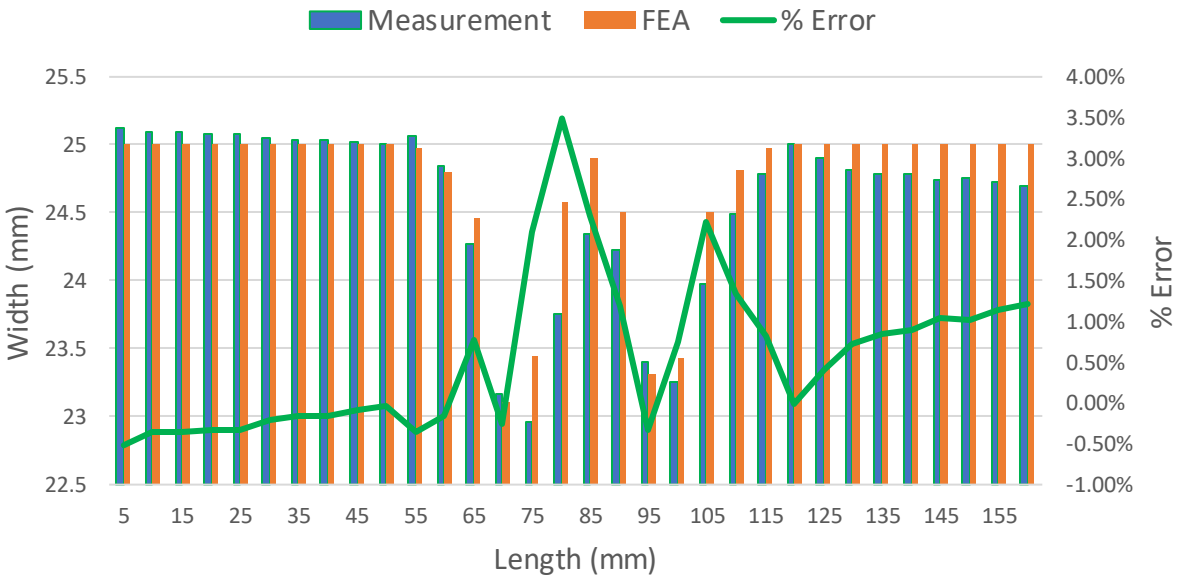

Figure 5.14 Comparison of calculated and measured width with % error

5.3. Calculation of thickness of FE beam and comparison with measurements

Calculating the beam's thickness is not a simple matter of taking the difference between the nodal coordinates. The width of the beam in the FE model aligns with the Z axis of the model's

global coordinate system. One edge aligns with Z=0 mm and the other edge aligns with Z=25 mm. For calculating thickness, the nodes considered are along the beam's centerline i.e. nodes at Z=12.5 mm. The list of nodes (created at the end of the stamping simulation) is imported into MATLAB and filtered to display only those nodes that fall on the beam's top and bottom surface and along its centerline. As shown in Figure 5.9 *Nodes on the top and bottom surfaces of the beam*, this produces a skeleton of the deformed beam where the nodes can be separated into two sets - ones on the top surface of the beam and ones on its bottom.

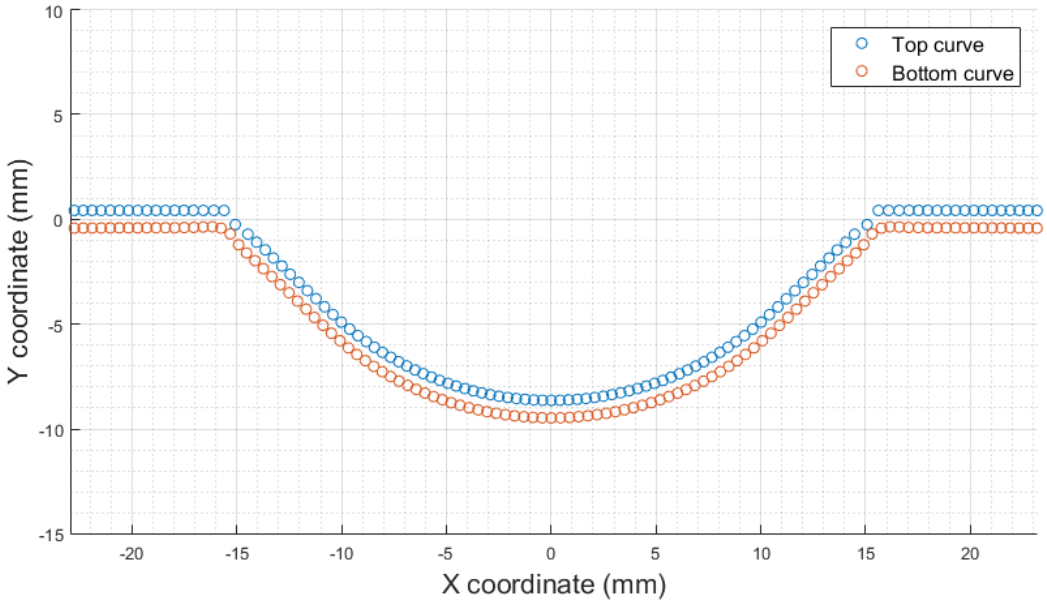

Figure 5.15 Nodes on the top and bottom surfaces of the beam

Each set can be further divided into a curved segment consisting of the dimple and two straight segments on either side of it. Curves are fit to these segments on both surfaces, with straight lines proving to be a good enough fit for the straight segments, while fifth order curves are found be the most accurate for the dimple. In Figure 5.10 *Simplified representation of dimple thickness calculation*

*Figure 5.11 Thickness calculation for every point along the dimple*Figure 5.10, the black circular arcs represent the top and bottom surfaces of the dimple. A tangent (green line) is drawn to the top curve at a node (point A) by taking the derivative of the curve's equation and using the

slope-point form of a straight line. Now, at the same node, a normal (blue line) is drawn to this tangent and the point of intersection of this normal and the bottom curve is found out (point B). The distance between points A and B is the thickness of the dimple. While Figure 5.10 *Simplified representation of dimple thickness calculation*

*Figure 5.11 Thickness calculation for every point along the dimple**Figure 5.10* is a simplified representation of this procedure, Figure 5.11 *Thickness calculation for every point along the dimple*

*Figure 5.12 Comparison of thickness calculated from FEA to its measured values**Figure 5.11* shows it done at every point on the dimple. In Figure 5.11 *Thickness calculation for every point along the dimple*

*Figure 5.12 Comparison of thickness calculated from FEA to its measured values**Figure 5.11*, nodes on the dimple are shown by circular markers, while the dashed lines are the curves fit to them. Also, every tangent and normal drawn at the same point has the same color so as be distinguishable from other tangent-normal pairs.

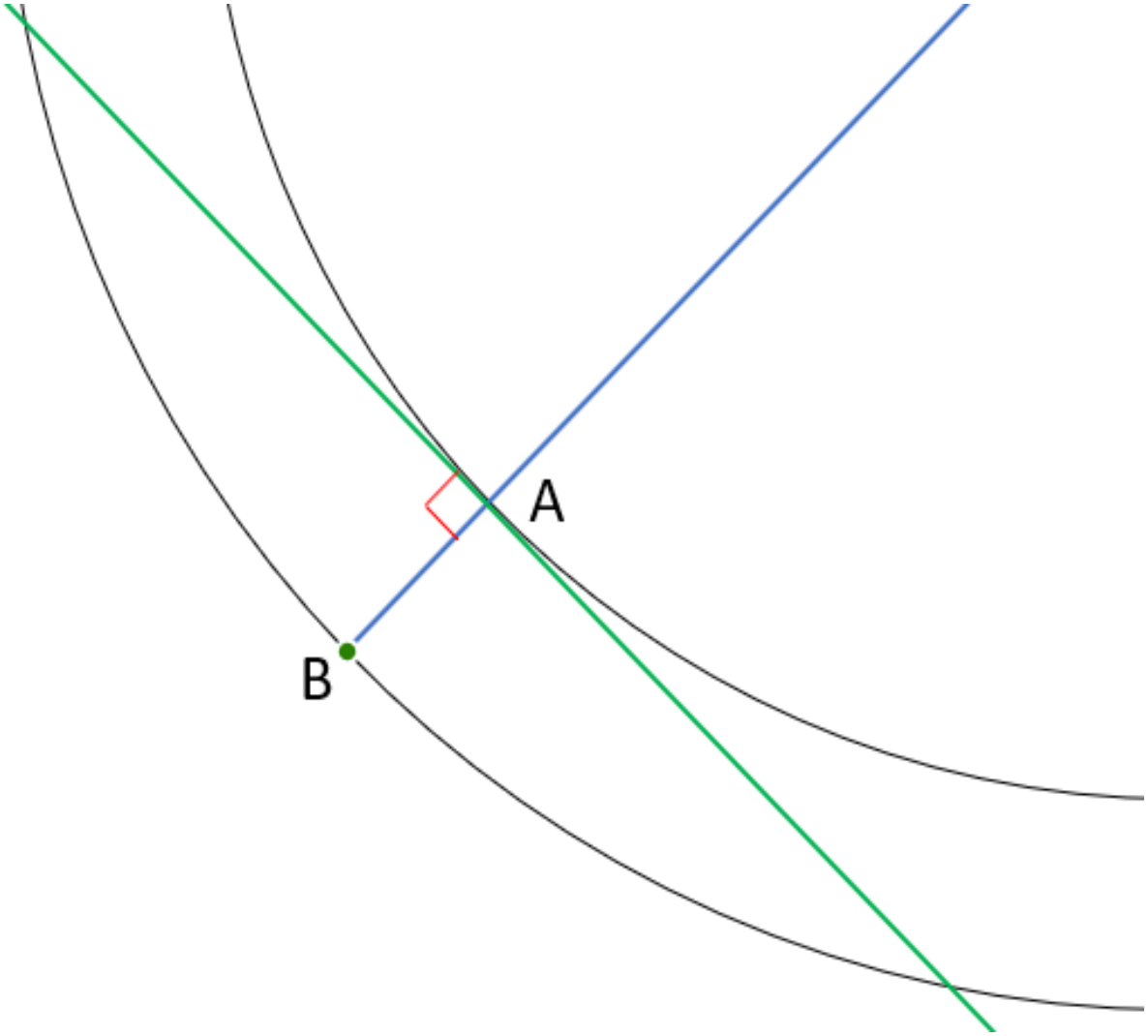

Figure 5.16 Simplified representation of dimple thickness calculation

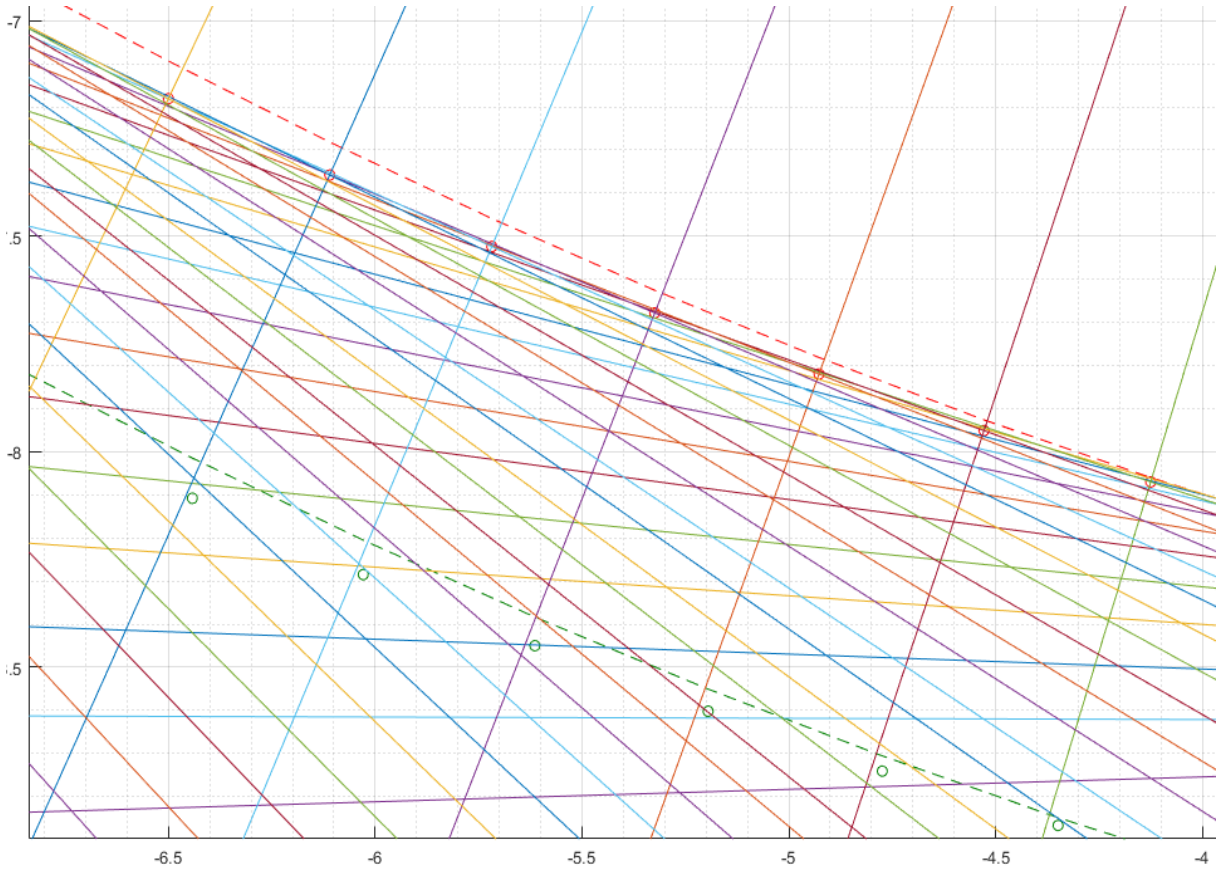

Figure 5.19 Thickness calculation for every point along the dimple

The thickness is calculated at every point along the curved and flat parts of the beam and then it is compared to the beam measurement values. Figure 5.12 *Comparison of thickness calculated from FEA to its measured values* shows this comparison while Figure 5.13 *Comparison of calculated and measured thickness with % error* adds % error to it. Both sets of data show similar trends, albeit with a lower degree of agreement than Figure 5.7 *Comparison of width calculated from FEA to its measured values*. This is evidenced by the higher % error values seen in Figure 5.13 *Comparison of calculated and measured thickness with % error* as compared to Figure 5.8 *Comparison of calculated and measured width with % error*. It must be noted however, that FEA data again shows greater variations than the measurements. Possible reasons for these trends and varying degrees of agreement are discussed in the next section.

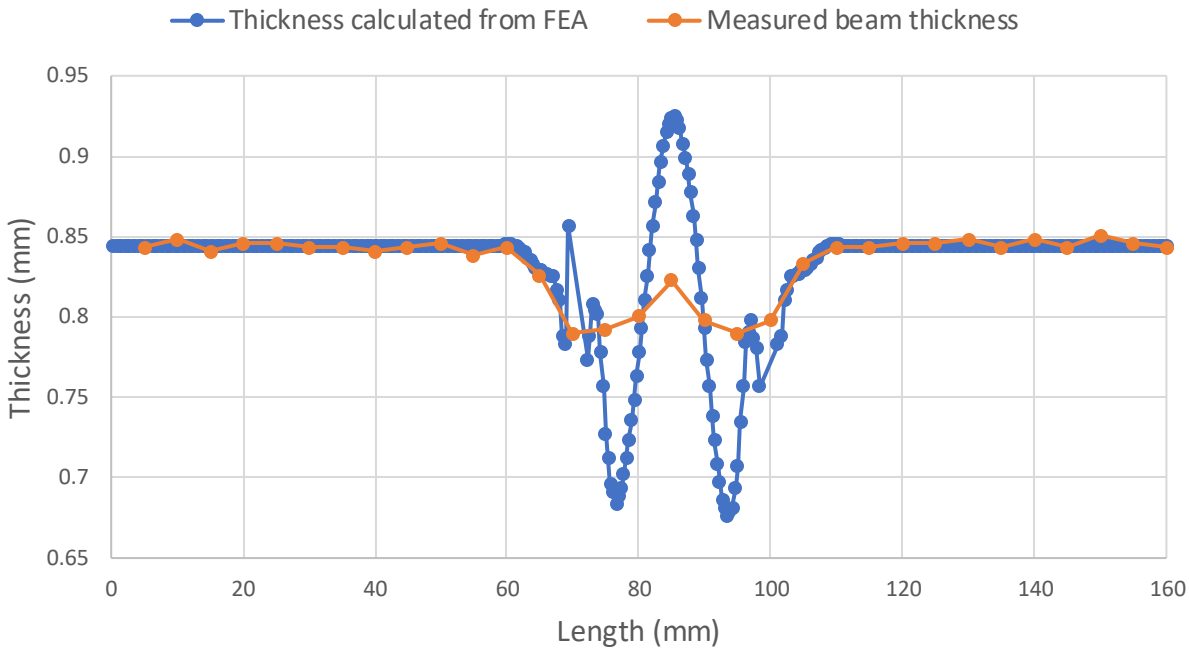

Figure 5.22 Comparison of thickness calculated from FEA to its measured values

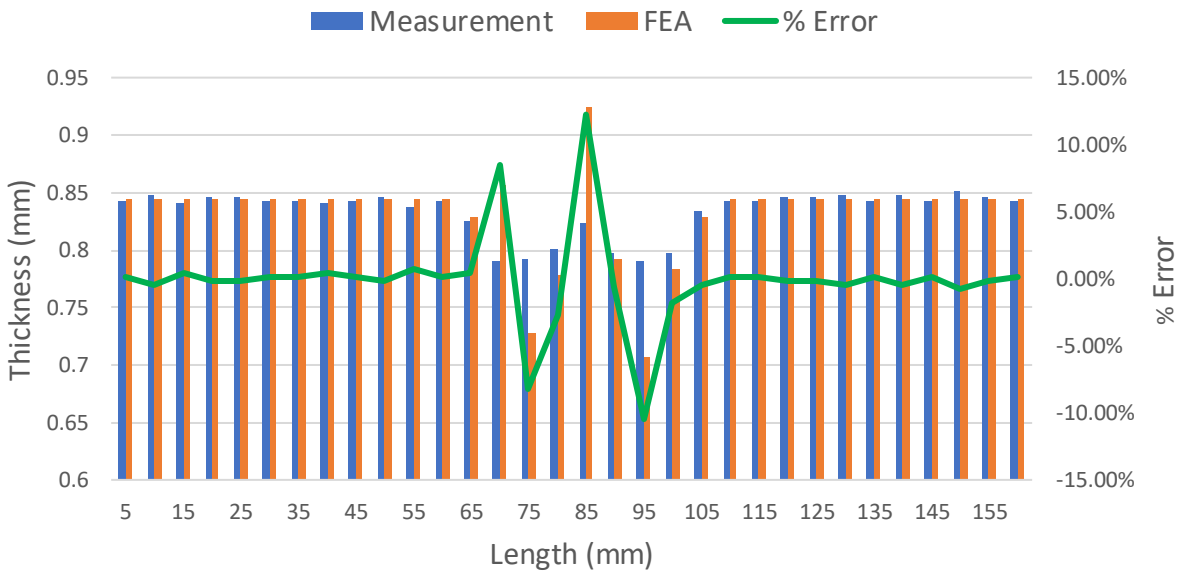

Figure 5.23 Comparison of calculated and measured thickness with % error

5.4. Explanation for differences between measurements and FE results

Figure 5.7 *Comparison of width calculated from FEA to its measured values*, Figure 5.8 *Comparison of calculated and measured width with % error*, Figure 5.12 *Comparison of thickness*

calculated from FEA to its measured values and Figure 5.13 *Comparison of calculated and measured thickness with % error* depict the comparison of data between the calculations from FE results and physical measurements of thickness and width. It was noted that both quantities followed similar trends. A downward trend was observed just before the dimple began. After reaching a low point, they gradually recovered culminating in a peak at the center of the dimple. But, the dip in the FE data was larger and so was the recovery. The primary point here is that although both sets of data follow similar trends, the magnitudes of their variations are significantly different.

The changes in the thickness and width can be ascribed to the strains that the beam undergoes after experiencing the downward motion of the plunger. When the plunger travels downward, it meets the beam at the would-be center of the dimple and pushes it down. This creates strains at unconstrained parts of the beam in the immediate vicinity of the clamps (i.e. the points where the dimple starts). This stretching of the beam along its length continues until the plunger reaches the farthest point of its downward travel. The plunger then retracts by moving in the opposite direction and the deformed dimple recovers some of the elastic fractions of the induced strains in what is known as 'spring back'. Thus, the stretching of the beam due to the motion of the plunger is the only source of strain in the model. Strain generated in the direction of the beam's length in this manner is transferred to the directions aligned with its thickness and width in the form of lateral strain. The proportion of this strain transferred as lateral strain is governed by the Poisson's ratio of the material [14, p. 93]. While the above explanation is theoretically sound, it leaves unexplained some of the differences observed between the FE data and the measurements. Evidently, both sets of data do not match perfectly and the reasons for those deviations will be enumerated and explored below.

5.4.1. Inaccuracies in curve fitting

As discussed in Section 5.3, a list of nodes with their coordinates is exported from the FE simulation, nodes corresponding to the top and bottom surfaces of the dimple are isolated separately and curves are fit to them. Unavoidable errors in this process of curve fitting produce some of the inaccuracies witnessed in earlier comparisons. But before proceeding, it is necessary to cover a couple of essential statistical terms. First off, the R-squared value, also known as the

coefficient of determination, is a measure of the closeness of the data to the curve fit to it. It is usually expressed as a percentage between 0 and 100 and high values of R-squared denote a good fit [18, p. 251]. Secondly, residuals are defined as the differences between the input data points and values predicted by curve fit [18, p. 80]. The curves fit to the data here have a very high R-squared value (over 99%). However, the curve encompasses points spread over a horizontal distance of around 50 mm and a vertical range of about 15 mm. By contrast, the thickness of the dimple is on the sub-millimeter scale. Thus, any inaccuracies in the curve fit, no matter how small, are still on the scale of the thickness. Figure 5.11 *Thickness calculation for every point along the dimple*

*Figure 5.12 Comparison of thickness calculated from FEA to its measured values*Figure *5.11* demonstrates this, where there is a visible offset between the circular markers representing the data points and the dashed line representing the curve fit to them.

Additionally, a closer inspection of the curve fitting procedure reveals that over one third of the points have residuals between 0.1 mm and 0.15 mm. While these are very small numbers in physical terms and within the scope of the curve fit, they are on the same order of magnitude as the flat beam's thickness of 0.844 mm. Thus, unintentional but inevitable numerical errors in curve fitting contribute to making the calculation of thickness slightly inaccurate.

5.4.2. Measurement errors

Another possible source of error is the measurement of dimple thickness using the point micrometer. It is crucial for the accuracy of the measurements that the micrometer is held perpendicular to the surface of the dimple. However, due to the very small thickness of the dimple, it is difficult to visually judge if this is indeed the case.

5.4.3. Friction

Friction in stamping is a significant yet undesirable factor in shaping the dimple. Its presence affects the way forces are transferred from the plunger to the beam. It also plays a pivotal role in the creation of local stresses and the resulting deformation. While a coefficient of friction has been specified as part of the input material properties, it is difficult to judge the effect

of friction on the mechanics shaping the deformation of the beam. Conceivably, a change in this value of the coefficient of friction could result in a change in the final shape of the dimple.

5.5. Summary

This chapter focused on the validation of results obtained from the finite element simulation of stamping. To that end, the thickness and width of the area of the beam surrounding the dimple were calculated. They were then compared with corresponding measurements made on the real beam. This yielded a mostly agreeable comparison where dominant trends in the measurements were seen to be replicated in the FE results as well.

As for the differences observed, reasoning was provided to account for them. The disproportionate nature of the dimple's length and thickness introduced inaccuracies into the curve fitting. Also, errors in the micrometer measurements and the unpredictability introduced by the presence of friction were some of the other causes for those differences.

However, the principal objective of this research is the investigation of the effect stamping has on the vibrational performance of dimpled beams. In line with that objective, it is necessary to evaluate whether the high accuracy of the results from the stamping simulation is a prerequisite for the accuracy of vibrational results. That is not the case as is proven by data presented in Chapter 8, where the natural frequency results from the FE model are compared to experimental values. Consequently, the present state of the stamping simulation is deemed sufficient.

6. Finite element simulation of beam vibrations

The purpose of this chapter is to describe how the results from experimental modal analysis are replicated using finite element (FE) simulation. This fairly straightforward process is detailed in Section 6.1, while Section 6.2 describes how the results are different from previous work in the theoretical domain.

6.1. FE modal analysis

The purpose of this research is to simulate and quantify the effects of a dimple with non-uniform thickness and width on the natural frequencies of a beam. As described in Chapter 4, the creation of such a dimple is attained by a static structural simulation of the stamping process. The output from that analysis is used as the starting point for this simulation. The deformed geometry of the beam from the final load step and the defined parameters are imported. It should be remembered here that this previous simulation had a beam and a plunger, the latter of which is no longer necessary. Hence, the plunger mesh and the underlying geometry are removed. In addition, the contact elements on the surfaces of the plunger and the beam are deleted as they are no longer required.

A host of boundary conditions can be implemented by selecting any end and applying the appropriate constraints. For example, a cantilever beam can be created by selecting nodes at one end of the beam and constraining all their degrees of freedom, while leaving the other end completely unconstrained. Figure 6.1 *First transverse mode of a cantilever beam (front view). Images used courtesy of ANSYS, Inc.*

Figure 6.2 First torsional mode of a cantilever beam (front view). Images used courtesy of ANSYS, Inc.Figure 6.1, Figure 6.2 *First torsional mode of a cantilever beam (front view). Images used courtesy of ANSYS, Inc.*

Figure 6.3 First lateral mode of a cantilever beam (top view). Images used courtesy of ANSYS, Inc.Figure 6.2 and Figure 6.3 *First lateral mode of a cantilever beam (top view). Images*

used courtesy of ANSYS, Inc. respectively show transverse, torsional and lateral mode shapes of a beam with a single dimple with cantilever boundary conditions (left end fixed, right end free). However, it must be noted that only transverse modes from the simulation will be used for model validation since the single-axis accelerometer used in the experimental setup only allows for detection of transverse modes.

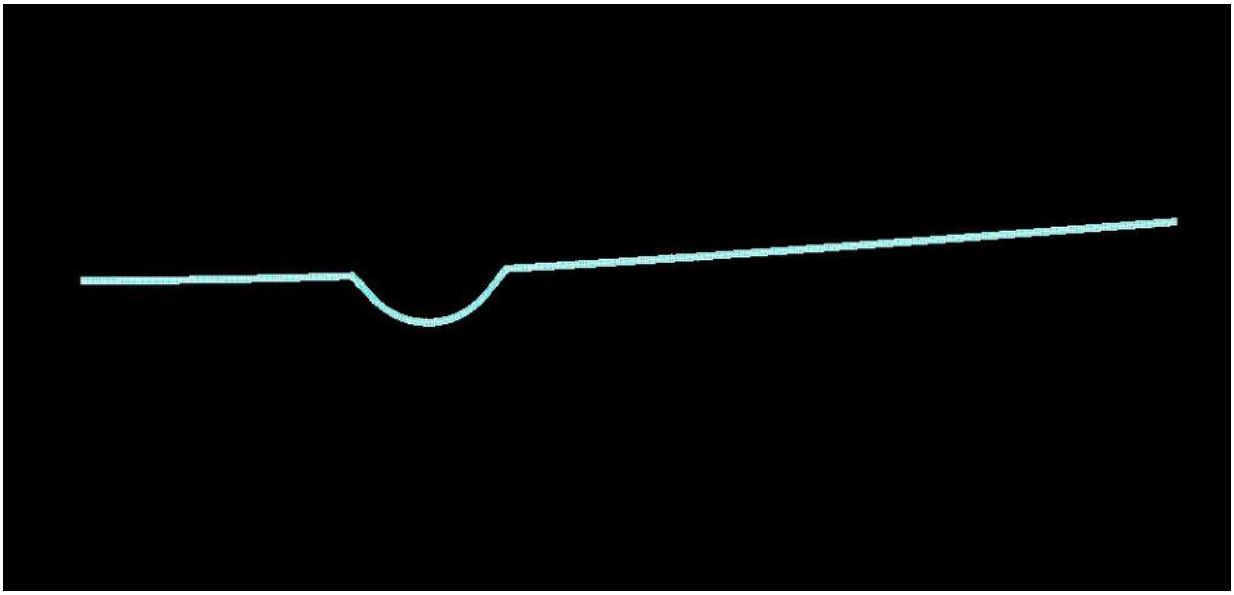

Figure 6.1 First transverse mode of a cantilever beam (front view). Images used courtesy of ANSYS, Inc.

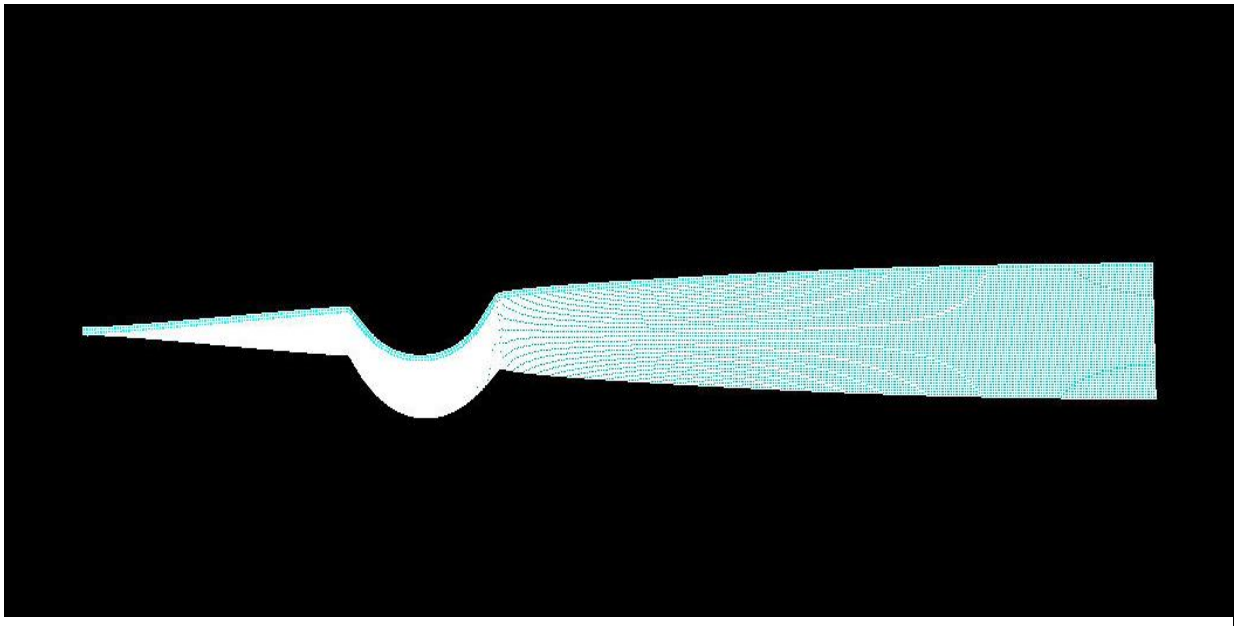

Figure 6.4 First torsional mode of a cantilever beam (front view). Images used courtesy of ANSYS, Inc.

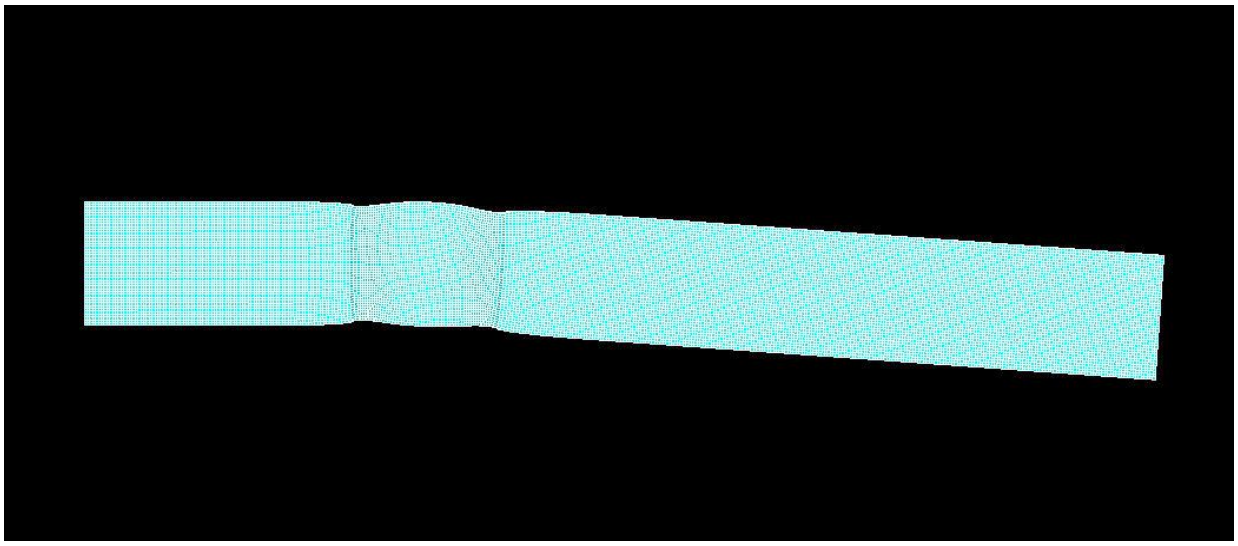

Figure 6.7 First lateral mode of a cantilever beam (top view). Images used courtesy of ANSYS, Inc.

6.2. Differences from previous theoretical work and summary

There are two major differences between this simulation and previous theoretical work [5], [6], [7]. Firstly, the model here is three-dimensional (3-D), while earlier models were two-dimensional (2-D) and did not have a width dimension. While this may not seem like a significant distinction, modelling the beam in three dimensions instead of two is a better approximation of reality and grants greater freedom to explore the ramifications of a non-uniform dimple. This

distinction also necessitates the use of a different kind of FE element. In building a 3-D model, solid elements exhibiting all three dimensions are used, whereas the 2-D model used beam elements lacking this capability. Therefore, this model can exhibit torsional as well as lateral modes in addition to regular transverse modes. On the other hand, the 2-D formulation lacks the ability to model non-transverse modes, let alone exhibit them. Also, the dimple shows variation in width in addition to its thickness, which the 3-D FE model accounts for too. All these factors contribute to making it more accurate and realistic.

7. Experimental modal analysis procedure

This chapter details the process of conducting the modal analysis experiment on dimpled beams. The purpose of the modal analysis is stated in Section 7.1, while Section 7.2 provides a brief introduction to the test apparatus. The procedure for the modal analysis itself is explained in Section 7.3 and precautions to be taken to ensure the reliability of the data are enumerated in Section 7.4. Finally, Section 7.5 offers a summary of the chapter. It must be noted that this chapter is dedicated to describing the experimental procedure only and the results and the subsequent analysis are provided in the next chapter.

7.1. Goal of modal analysis

The purpose of this experiment is to extract natural frequencies of beams, which can then be compared with the results from the finite element (FE) simulation. This comparison will yield insights into the degree of agreement between the two and allow assessment of the accuracy with which the simulation captures the various aspects of the physical experiment.

Previous researchers have gathered data for two-dimpled beams with fixed-fixed and fixed-free boundary conditions [5], [7]. However, results generated for those end conditions using the FE methodology described in this work were ambiguous enough to not be able to make a supportable inference about the accuracy of those methods. This was primarily because of the difficulties faced in recreating a 'fixed' boundary condition[1]. Ideally, a fixed boundary condition is a surface which is infinitely rigid (has an infinite mass) and exhibits no coupling whatsoever with the structure attached to it. As both conditions are very difficult to fulfill in practice, it was decided that the free boundary condition would be used for the experiment due to its ease of implementation. These changes made the measurements less error-prone and strengthened the conclusions drawn by comparing them to FE results. Three kinds of beams - with a single dimple, with two dimples both facing the same way and with two dimples facing opposite directions - were used. Their dimensions are given in Table 7.1, Table 7.2 and Table 7.3.

[1] While Alshabatat [5], Myers [6] and Ghazwani [7] did face this hurdle, achieving an exact match between FE results and experimental values was not one of their research objectives. Also, they could attribute the discrepancies to the fact that the dimples they modeled were not an accurate representation, but rather an approximation.

Table 7.1 Dimensions of beam with a single dimple[2]

Parameter	Value
First segment length	135 mm
Location of dimple center	150 mm
Second segment length	135 mm
Total beam length	300 mm
Beam width	25 mm
Flat beam thickness	0.84 mm
Dimple angle	135°

[2] Locations of dimple centers are specified as distances from one end of the beam, while dimensions of flat segments are specified simply as their lengths, independent of any point of reference.

Table 7.2 Dimensions of a beam with two dimples in opposite directions[2]

Parameter	Value
First segment length	45 mm
Location of first dimple center	60 mm
Second segment length	65 mm
Location of second dimple center	155 mm
Third segment length	132 mm
Total beam length	302 mm
Beam width	26 mm
Flat beam thickness	1.15 mm
Dimple angle 1	135°
Dimple angle 2	135°

Table 7.3 Dimensions of a beam with two dimples in the same direction[2]

Parameter	Value
First segment length	45 mm
Location of first dimple center	60 mm
Second segment length	65 mm
Location of second dimple center	155 mm
Third segment length	130 mm
Total beam length	300 mm
Beam width	25.8 mm
Flat beam thickness	1.15 mm
Dimple angle 1	135°
Dimple angle 2	135°

7.2. Equipment used for modal analysis

The measuring instruments used are an impact hammer and an accelerometer. Figure 7.1 *Experimental setup (partial)* shows a part of the experimental setup. The flat beam, with an accelerometer (blue cable) attached to it, is suspended from table clamps using rubber bands to create free boundary conditions at both ends. Not shown in the picture are the impact hammer and the data acquisition module connecting the instruments to the software used for the measurements. Both measuring instruments are equipped with piezoelectric sensors, meaning

they convert their respective measured quantities (force for the impact hammer and acceleration for the accelerometer) into output voltage signals. They are connected to m+p Analyzer software from m+p International via a National Instruments data acquisition module. Figure 7.2 *Flow of data from measuring instruments to the analysis software* is a schematic illustration of this arrangement. A list of the apparatus used along with a brief description for each component is provided below.

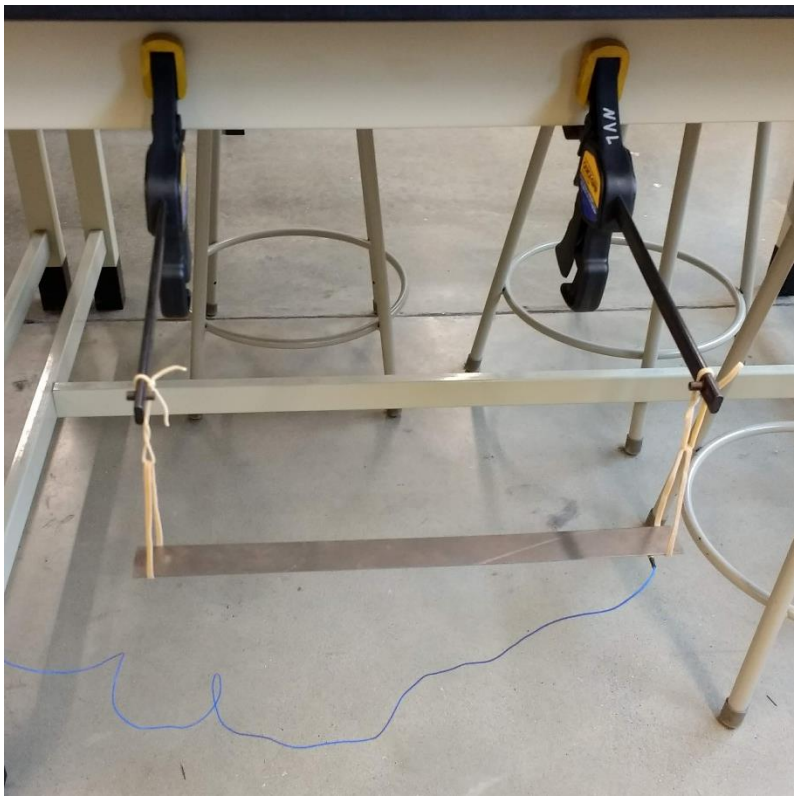

Figure 7.1 Experimental setup (partial)

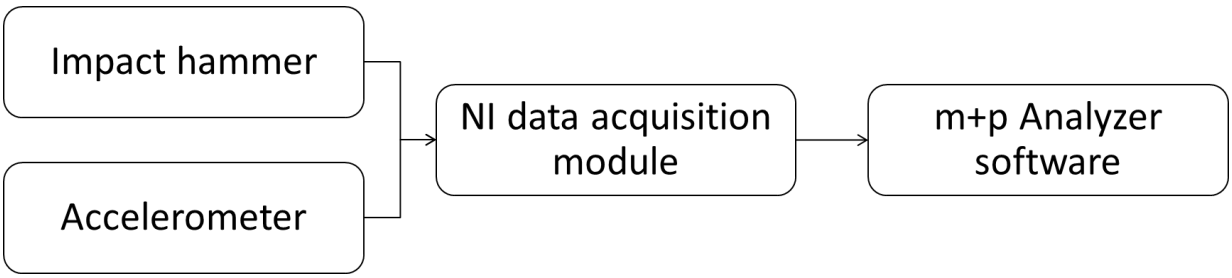

Figure 7.2 Flow of data from measuring instruments to the analysis software

7.2.1. Impact hammer

A PCB Piezotronics model 086C04 impact hammer is used to provide the excitation input to the structure for this experiment. It is connected via BNC cables to the NI-9234 data acquisition card. It has a force sensor integrated into its striking surface, which measures the amplitude and frequency of the impact generated along the axis of the hammer tip. A tip fitted onto this sensor affects how the force impulse generated by the hammer's impact is transmitted to the beam. For instance, a soft tip would excite the low frequency modes of the beam, while a hard tip would excite the high frequency ones. Since the frequencies corresponding to the first few transverse modes of vibration are of interest here, a soft tip is used. A picture of the hammer, with the tip used, is shown in Figure 7.3 *PCB Piezotronics model 086C04 impact hammer (with blue rubber tip)* and its key specifications are given in Table 7.4 [19, p. 43].

Figure 7.3 PCB Piezotronics model 086C04 impact hammer (with blue rubber tip)

Table 7.4 Key specifications for impact hammer

Parameter	Value
Sensitivity	1.1 mV/N (±15%)
Measurement range	±4448 N peak
Hammer Mass	0.16 kg

7.2.2. Accelerometer

An accelerometer measures acceleration directly caused by the response of the underlying structure to the excitation force imparted by the impact hammer. For this experiment, a PCB model 352C22 single axis miniature piezoelectric accelerometer is used. It has a ceramic sensing element and measures the structure's response in the direction perpendicular to the surface to which it is attached. Figure 7.4 *PCB model 352C22*

Figure 7.5 National Instruments (NI) data acquisition module *Figure 7.4* shows a picture of the accelerometer with Table 7.5 summarizing its key specifications [19, p. 12].

Figure 7.4 PCB model 352C22

The choice of this accelerometer is based on two factors. Firstly, its capability for data collection along a single axis allows it to pick up the structure's response corresponding only to its transverse modes of vibration, while leaving out torsional and lateral vibrations and random noise. Secondly, since it weighs only half a gram, it adds practically no weight to the beam and consequently, will have minimal effect on dynamic behavior of the beam.

Table 7.5 Key specifications for accelerometer

Parameter	**Value**
Sensitivity	10 mV/g (±15%)
Measurement range	±500 g peak
Broadband resolution	0.004 g RMS
Frequency range	1 to 10000 Hz (±5%)

7.2.3. Accelerometer calibrator

It is imperative that the accelerometer be calibrated before it is used to ensure that the data collected is accurate. PCB model 394C06 is a battery-powered handheld shaker designed specifically to evaluate accelerometer performance and is used for accelerometer calibration. It emits an acceleration signal of magnitude of 9.81 m/s^2 (1 g) rms at a frequency of 1000 rad/s (159.2 Hz). Considering the accelerometer sensitivity of 10 mV/g with a margin of ±15%, it should respond to an input signal of 1 g with an output signal in the range of 8.5 mV to 11.5 mV.

7.2.4. m+p Analyzer software

m+p Analyzer, a dynamic signal analysis software provided by m+p International, is used for storing, viewing, analyzing and post-processing data acquired through the measurement channels [20]. It interfaces effortlessly with the measurement hardware and allows real-time viewing of data. One of its features particularly well-suited for modal analysis is that it displays a warning if double impact is detected, which eliminates a major source of error as described in Section 7.4.2. Also, it converts time record data into the frequency domain instantly and shows the FRF as well as coherence.

7.2.5. Data acquisition module

The data acquisition module from National Instruments (NI) shown in Figure 7.5 *National Instruments (NI) data acquisition module* consists of a model 9162 USB carrier and a model 9234 four-channel data acquisition card. It acquires voltage signals from both the impact hammer and the accelerometer, conditions them and transmits them to the software for viewing and post-processing.

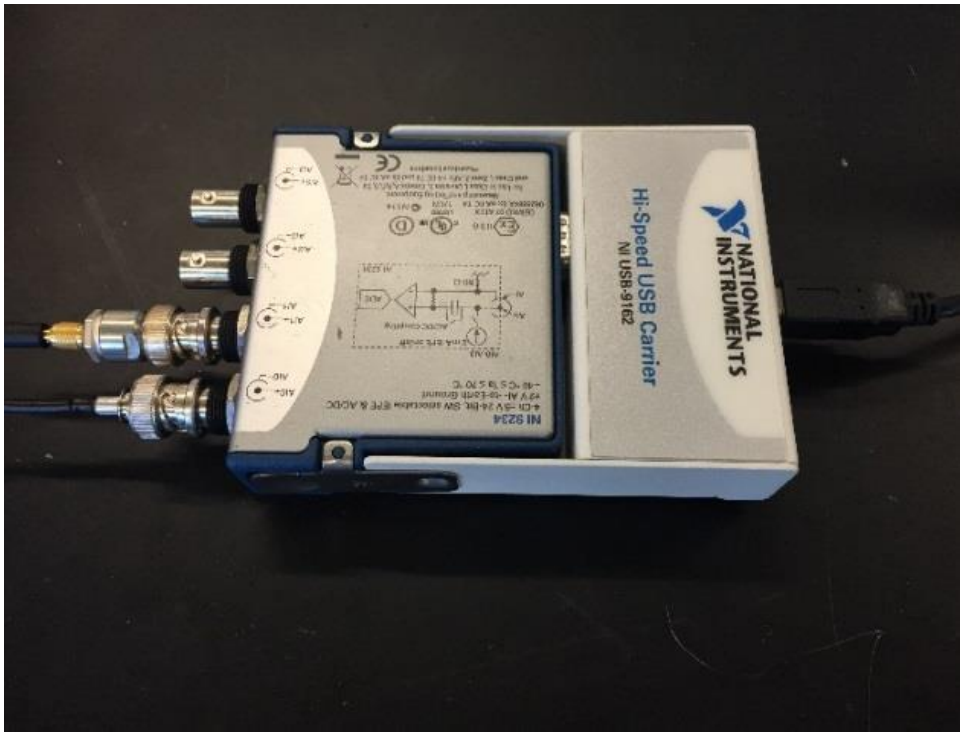

Figure 7.7 National Instruments (NI) data acquisition module

7.3. Experimental procedure

The first step in the measurement procedure is the calibration of the accelerometer. This is done by attaching it to the calibrator which generates a 1 g RMS acceleration signal. After ensuring satisfactory performance of the accelerometer, it is attached to one end of the beam using beeswax. Next, a simplified model of the beam is built in the modal analysis software. The coordinates of the points on the beam where it will be struck are specified. Three measurements are made at each of these points and their average is used in the final analysis.

The last step before making the actual measurements is setting up the beam boundary conditions. As mentioned in Section 7.1, free boundary conditions were used. Ideally, that would mean the structure is freely suspended without any constraints. In practice, this is achieved by a suspension system whose stiffness, as a rule of thumb, is at least an order of magnitude lower than that of the structure itself. In the present scenario, the beam itself is relatively lightweight and rubber bands suspended from the arms of bar clamps proved to be adequate. However, a single rubber band at either end was deemed too flexible and sensitive, so two rubber bands

acting as springs in parallel were used, as shown in Figure 7.6 *Creation of free-free boundary conditions for a flat beam*

Figure 7.7 Frequency Response Function (FRF) with peaks signifying natural frequenciesFigure 7.6.

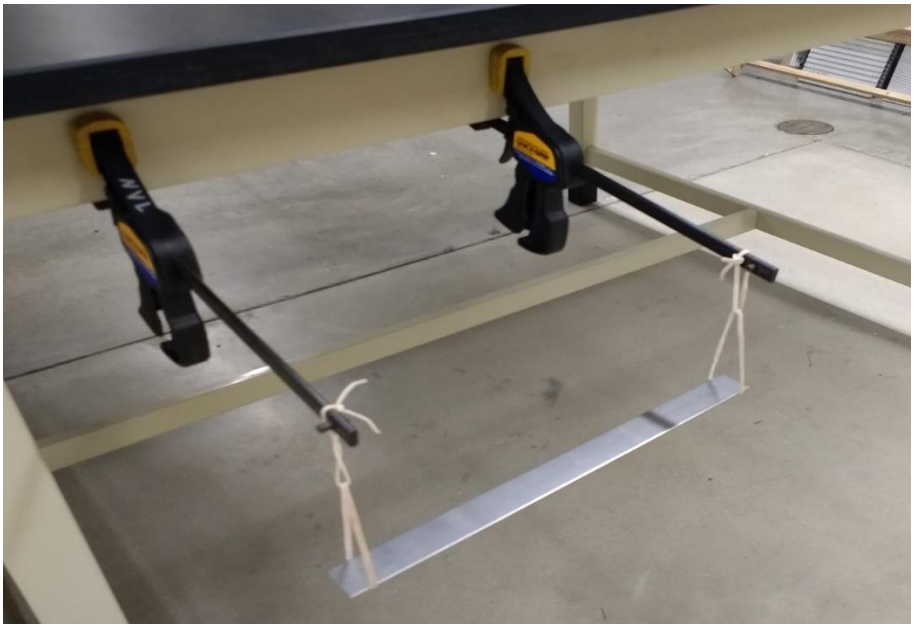

Figure 7.8 Creation of free-free boundary conditions for a flat beam

With the experimental setup in place, the beam was struck at three predetermined locations along its length. The data collected by the accelerometer and the impact hammer are then used to calculate the frequency response function (FRF). In essence, the FRF is the ratio of the acceleration response of the structure to the force imparted by the hammer over the frequency range of interest. A sample FRF is shown in Figure 7.7 *Frequency Response Function (FRF) with peaks signifying natural frequencies*. At points of structural resonances, the graph shows peaks signifying a greater magnitude of response. The natural frequencies of the structure can be obtained by observing the frequencies at which these peaks occur in the FRF.

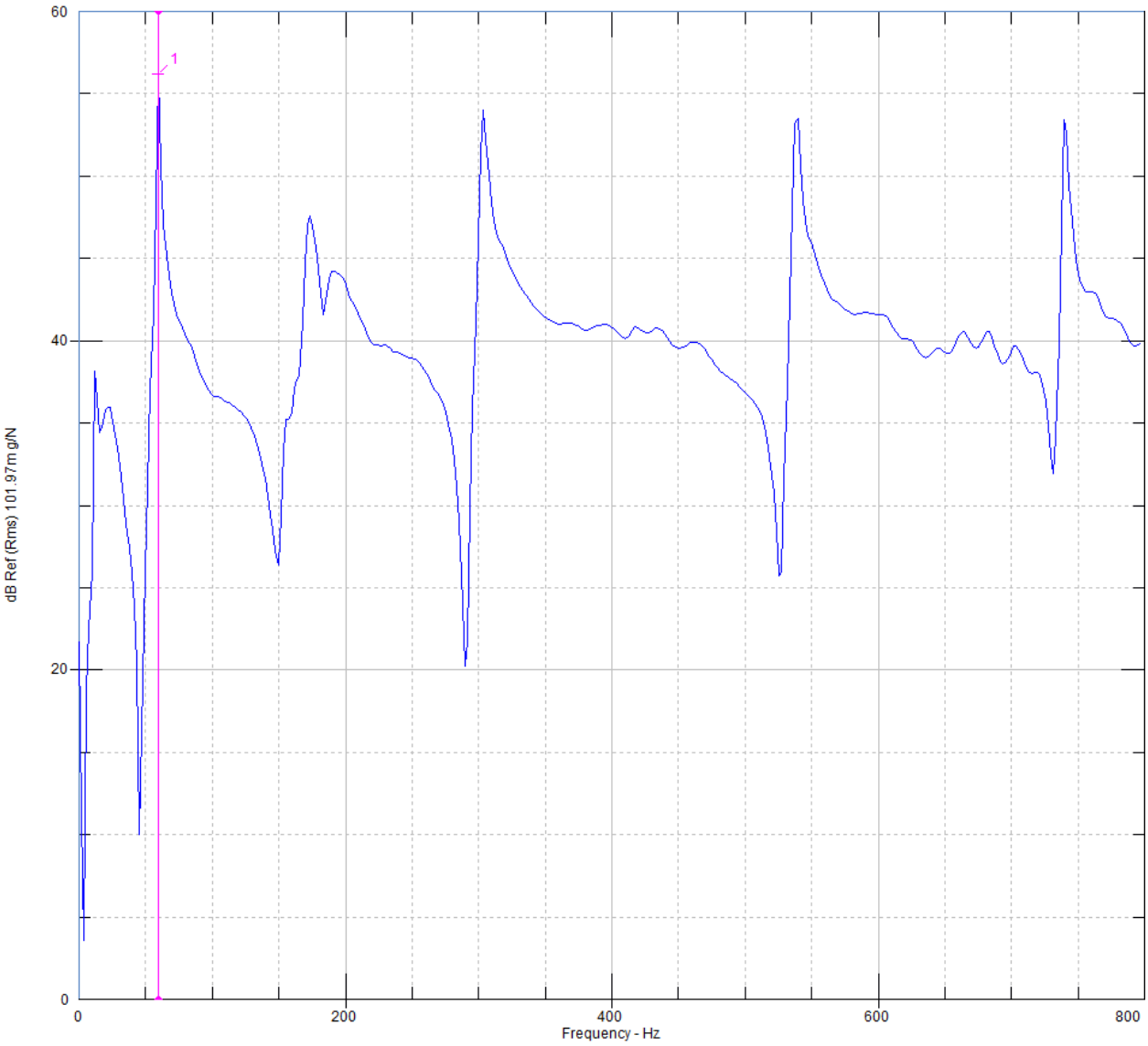

Figure 7.11 Frequency Response Function (FRF) with peaks signifying natural frequencies

7.4. Precautions to be taken while making measurements

While conducting a modal analysis test, precautions must be taken to ensure that the data collected is accurate and reliable. They are enumerated below.

7.4.1. Location and direction of impact

The location of impact should be kept as close as possible to the beam's centerline and the angle of impact must be perpendicular to its surface in order to avoid axial, lateral or torsional movement. This is limited by the experimenter's ability to correctly hit the same spot on the beam multiple times.

7.4.2. Double impact

During this experiment, one must be careful to avoid double impact, which is defined as subjecting the beam to more than one strike from the hammer in quick succession. When the hammer strikes the beam, there is small local elastic deformation at the point of contact. The restorative force of the material causes the beam to spring back and it hits the hammer if it is still there. As all of this happens over a period of a few milliseconds, the hammer should strike the beam and be withdrawn in one quick motion. As mentioned in Section 7.2.4, the measurement software can detect double impact and instantly provides the opportunity to redo that particular measurement.

7.4.3. Coherence

Coherence is a measure of the quality of measurements made. It quantifies how much of the measured response is caused by the excitation. Its value ranges between 0-1 and a good measurement is signified by a coherence value close to one over the entire frequency range of interest. Conversely, a lack of this behavior means a measurement does not have good coherence. Nevertheless, a measurement with good coherence will show dips at frequencies corresponding to its resonances. It is also acceptable for coherence to be low at anti-resonances or structural nodes as the response is very low at those points. Figure 7.8 *Example of good coherence with the dips signifying resonances*

Figure 7.9 Example of bad coherence with resonances completely indistinguishableFigure 7.8 and Figure 7.9 show examples of good and bad coherence. Note that the dips signifying resonances cannot be distinguished in Figure 7.9.

Figure 7.12 Example of good coherence with the dips signifying resonances

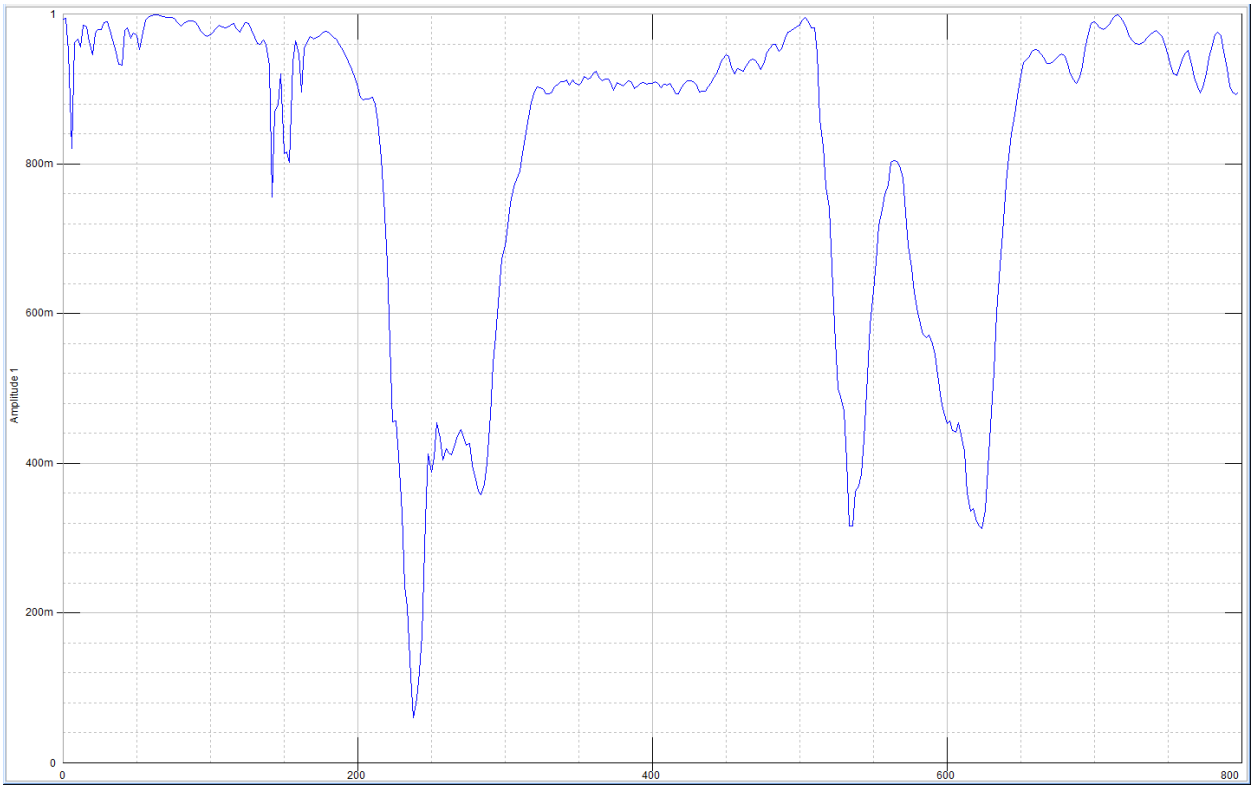

Figure 7.15 Example of bad coherence with resonances completely indistinguishable

7.4.4. Other forms of error

Despite best efforts, error inevitably creeps into the measurements. Several instruments, each with its own resolution and calibration are involved, and introduce a tiny measure of unreliability to the results. Also, erroneous handling of the instruments and mistakes in reading and/or interpreting the results on the experimenter's part also have an effect. Then there is random error, whose influence can be alleviated by repeating the measurements several times and using statistical methods to make sure they are not too far spread out. Thus, any error in the experiment from causes other than the above can be collectively put down to some combination of systematic, human and random error.

7.5. Summary

Dimensions for the beams used in the experiment were given and equipment like the impact hammer, accelerometer, calibrator and the software were described. Later, the procedure itself was explained followed by measures to take to ensure the repeatability and accuracy of the data collected.

8. Validation of results from finite element modal analysis

The focal point of this chapter is the examination of the values of natural frequencies obtained from the FEA presented in this work. In Section 8.1, their agreement with the experiment and the Boundary Value Model (BVM) is examined. Next, it was mentioned in Section 4.2.1 that the material stress-strain behavior obtained from tension testing can be used in FEA via two kinds of implementations. Results obtained from both of those approaches are evaluated in Section 8.2. It must be noted here that results presented in Section 8.1 were generated using the first approach (Negative slope avoidance method 1, Figure 4.4 *Negative slope avoidance method 1*

Figure 4.5 Negative slope avoidance method 2Figure 4.4). Section 8.3 briefly summarizes key observations made from all the presented data.

8.1. Validation of results

All experimentation presented here for the purpose of comparison with FE results utilized free boundary conditions at both ends of the beam. The experiments were carried out on a beam with a single dimple and beams with two dimples in the same and opposite directions. The dimensions for these beams were given in Table 7.1, Table 7.2 and Table 7.3. These comparisons are shown in Table 8.1, Table 8.2 and Table 8.3. In addition to the values of natural frequencies, these tables provide a measure of error with respect to the experimental values in the form of percent difference, which is calculated with the following formula.

$$\%\ \text{difference} = \frac{\text{FEA (or BVM) results-Experimental values}}{\text{Experimental values}} \times 100\% \qquad (8.1)$$

Table 8.1 Comparison of natural frequencies from FEA to experimental values for a free-free beam with a single dimple

Frequency	Experimental values (Hz)	FEA results (Hz)	% difference
1	47.36	44.238	-6.59%
2	128.65	131.38	2.12%
3	251.42	244	-2.95%
4	425.16	418.53	-1.56%
5	564.91	554.62	-1.82%

Table 8.2 Comparison of natural frequencies from FEA to experimental values for a free-free beam with two dimples in opposite directions

Frequency	Experimental values (Hz)	FEA results (Hz)	% difference
1	59.91	58.621	-2.15%
2	174.92	164.25	-6.10%
3	303.84	307.29	1.14%
4	538.97	539.03	0.01%
5	740.92	754.39	1.82%

Table 8.3 Comparison of natural frequencies from FEA to experimental values for a free-free beam with two dimples in the same direction

Frequency	Experimental values (Hz)	FEA results (Hz)	% difference
1	60.46	59.315	-1.89%
2	173.11	167.17	-3.43%
3	319.32	319.87	0.17%
4	509.1	510.29	0.23%
5	676.68	746.72	10.35%

Table 8.1 shows that except for the first frequency, the difference is less than 3%. The numerical error for the first frequency is relatively small (≈3 Hz), but the % difference figure appears inflated because of the relatively small base used for the comparison (47.36 Hz). In Table 8.2, all values of % difference are very close to or less than 2%. Of note is the fourth frequency where both values are practically the same. A major deviation is seen in the second frequency where the % difference is 6.1%. For a beam with two dimples in the same direction, the first four frequencies exhibit less than 3.5% difference. Importantly, the third and fourth frequencies practically coincide with their experimental counterparts. With the fifth frequency, the margin of error is relatively large at 10.35%. However, upon closer inspection of the experimental data corresponding to that mode, it was seen that the coherence for that data point is not as good as the previous points. Hence, the experimental value of the frequency is slightly less reliable. Overall, the averages of the % differences shown in Table 8.1, Table 8.2 and Table 8.3 are -2.16%, -1.06% and 1.09% respectively. Based on this data, it can be concluded that predictions of natural frequencies of dimpled beams produced by the FE model are highly accurate and agree very well with experimental results.

The reasons for the agreement exhibited between the simulation and experimental results are twofold. First, the modal analysis that generated the natural frequency results was conducted on the output of the stamping simulation. So, the overall shape and variations

observed in the experimental beam were replicated in the FE model too. Secondly, tension testing of the beam material provided data and insight into its stress-strain behavior. The effective incorporation of this behavior into the FE model aided its accuracy and reliability.

Next, results from the FEA are also compared to those from the BVM in Table 8.4, Table 8.5 and Table 8.6. It is worth remembering that the BVM assumes a dimple with uniform thickness, whereas the FEA presented here makes no such assumption.

Table 8.4 Comparison of natural frequencies of experimental values to FEA and to BVM values for a free-free beam with a single dimple

Frequency	FEA results (Hz)	% difference	BVM results (Hz)	% difference
1	44.238	-6.59%	40.295	-14.92%
2	131.38	2.12%	129.931	1.00%
3	244	-2.95%	226.589	-9.88%
4	418.53	-1.56%	408.422	-3.94%
5	554.62	-1.82%	471.405	-16.55%

Table 8.5 Comparison of natural frequencies of experimental values to FEA and to BVM values for a free-free beam with two dimples in opposite directions

Frequency	FEA results (Hz)	% difference	BVM results (Hz)	% difference
1	58.621	-2.15%	53.088	-11.39%
2	164.25	-6.10%	154.802	-11.50%
3	307.29	1.14%	268.22	-11.72%
4	539.03	0.01%	498.922	-7.43%
5	754.39	1.82%	658.532	-11.12%

Table 8.6 Comparison of natural frequencies of experimental values to FEA and to BVM values for a free-free beam with two dimples in the same direction

Frequency	FEA results (Hz)	% difference	BVM results (Hz)	% difference
1	59.315	-1.89%	53.088	-12.19%
2	167.17	-3.43%	155.816	-9.99%
3	319.87	0.17%	281.027	-11.99%
4	510.29	0.23%	439.904	-13.59%
5	746.72	10.35%	615.421	-9.05%

Data presented in Table 8.4, Table 8.5 and Table 8.6 show that the FEA-based methodology in this research yields results that are more accurate than the BVM used by Alshabtat [5], Myers [6] and Ghazwani [7]. There are, however, two exceptions to this. For the second frequency of the single dimpled beam, the % difference for the FEA and BVM is 2.12% and 1% respectively. Although the BVM appears to be more accurate, the numerical error for the FEA is less than 3 Hz. Therefore, it would be unwise to judge the FEA to be less accurate just based on this comparison. The second exception is the fifth frequency for the beam with two dimples in the same direction. However, this frequency was discussed before and the experimental result was deemed less reliable on account of it having lesser coherence than other points of measurement. Another metric to compare the accuracies of both methods would be the average of their respective % differences for each kind of dimpled beam. This is given in Table 8.7.

Table 8.7 Comparison of average % difference for results from FEA and BVM

Type of beam	Average % difference for FEA results	Average % difference for BVM results
Single dimple	-2.16%	-8.86%
Two dimples in opposite directions	-1.06%	-10.63%
Two dimples in same direction	1.09%	-11.36

From Table 8.7, it can be surmised that FEA simulation described in this thesis is clearly superior to BVM as far as accuracy of frequency prediction is concerned. This superiority stems from the fact that the procedure followed in the FEA has several realistic aspects to it. Most importantly, the FEA considers the variations in cross-section of the beam and the dimple(s) as well as changes in their stiffness as outcomes of the stamping process. The BVM, on the other hand, tries to account for the variations in cross-section by assuming reduced, but uniform dimple thickness. To elaborate further on the FEA considering changes in stiffness, an interesting observation can be made from the data presented in Table 8.4 through Table 8.7. They show that the BVM always underestimates the beams' natural frequencies. This can be related to the fact that natural frequency is directly proportional to the square-root of the structure's stiffness [21]. Strain hardening occurring during stamping increases the beam's stiffness and hence, increases its natural frequencies. This is considered in the FEA and is one of the reasons its results are close to the experiment's. Due to the absence of any mechanism to account for this in the BVM, it predicts natural frequencies based on the stiffness of the undeformed beam and consequently, underestimates those values.

8.2. Comparison of results from different implementations of stress-strain data

As explained in Section 4.2.1, there are two ways of using the stress-strain data obtained from the tension test of the beam material. These have been illustrated in Figure 4.4 *Negative slope avoidance method 1*

Figure 4.5 Negative slope avoidance method 2Figure 4.4 and Figure 4.5 *Negative slope avoidance method 2*

Figure 4.6 Finite element model of beam and plunger after meshing. Images used courtesy of ANSYS, Inc.Figure 4.5. With all other parameters held constant, application of these two strategies yield slightly different natural frequency results as summarized in Table 8.8. The % difference shown is calculated using Equation (*8.1*.

Table 8.8 Comparison of results from two different implementations of stress-strain data

Type of beam	Frequency	Method 1	% difference	Method 2	% difference
Single dimple	1	44.238	-6.59%	44.285	-6.49%
	2	131.38	2.12%	131.42	2.15%
	3	244	-2.95%	243.75	-3.05%
	4	418.53	-1.56%	418.93	-1.47%
	5	554.62	-1.82%	550.11	-2.62%
Two dimples in opposite directions	1	58.621	-2.15%	58.697	-2.02%
	2	164.25	-6.10%	167.09	-4.48%
	3	307.29	1.14%	303.08	-0.25%
	4	539.03	0.01%	531.26	-1.43%
	5	754.39	1.82%	751.08	1.37%

Two dimples in same direction	1	59.315	-1.89%	59.885	-0.95%
	2	167.17	-3.43%	169.43	-2.13%
	3	319.87	0.17%	315.53	-1.19%
	4	510.29	0.23%	510.06	0.19%
	5	746.72	10.35%	701.78	3.71%

For a beam with a single dimple, the first four natural frequencies are practically the same. The fifth frequency is a bit different, but a change of 4 Hz for frequencies around 550 Hz cannot be considered significant. The differences are noticeable for a beam with two dimples in opposite directions. Except for the fourth frequency, method 2 seems to provide more accurate predictions. The effect is most significant for frequencies of a beam with both dimples in the same direction. Method 2 yields slightly better results apart from the third frequency. The only difference between both methods is the material behavior around the points of yield. In method 1, the stress-strain curve has a slope slightly greater than zero and the material offer little resistance to deformation. In method 2, on the other hand, the material yields at a lower value of stress, but provides steady resistance to deformation. Clearly, both methods' implementations of the material stress-strain data lead to slightly different results for natural frequencies. However, it is difficult to estimate the direct impact of these dissimilarities on the vibrational behavior of the beam and further investigation is required to explain the reasoning for these observations.

8.3. Summary

Natural frequencies of free-free beams with a single dimple, two dimples in opposite directions and two dimples in the same direction were calculated using the FE methodology presented here and compared with experimental results. In each instance, the average error in the FEA results was found to be less than 2.5%, suggesting good agreement between both sets of data. These FEA results were also compared with frequencies given by the Boundary Value

Model (BVM). For every case investigated, the prediction accuracy of the FEA was found to be at least four times better as compared to the BVM (Table 8.7).

It had been noted earlier that the material stress-strain data obtained from tension testing could be used in two ways in the FEA. Natural frequency results were generated using both approaches and their accuracy was compared with each other and experimental results. No method was found to have a clear advantage over the other in terms of accuracy of frequency prediction. However, further research into their physical implications and impact on deformation mechanics and vibrational behavior of the beam is needed.

9. Conclusions and future work

This chapter serves to bookend the main body of this thesis. A summary of all the findings is presented here and conclusions are drawn in Section 9.1. Thereafter, ideas for future research in this domain are provided in Section 9.2.

9.1. Summary and conclusions

It was stated in Chapter 1 that the objective of this research was to investigate the effect of stamping on the natural frequencies of dimpled beams. The first step towards that goal was taken by describing the physical setup used to create dimples on beams in Chapter 2. While the simplicity of its operation was noted, improvements were suggested to improve its flexibility and control over the process of dimple creation. The fixed distance between the clamps entails the use of a set plunger size. This limits all dimples created to a specific chord length. Also, the operator has no way of measuring the distance travelled by the plunger and in turn, the height of the dimple, meaning precise control cannot be exercised over the dimple size.

Next, stamping was to be simulated using finite element (FE) software. However, to better understand and encapsulate the stress-strain behavior of the beam material, tension testing was performed. The manufacturing of the test specimen, the test itself and calculation of material properties from the results were explained in Chapter 3. This was followed by a description of the FE simulation of stamping in Chapter 4. A deep understanding of the process was developed by assessing the mechanics of beam deformation and the constraints imposed by the stamping setup. Considerable effort went into the study of pivotal aspects such as strain hardening, plastic deformation, the role of contact, meshing etc. and their incorporation into the FE simulation.

The validation for this structural FE model with the aid of measurements performed on dimpled beams was provided in Chapter 5. Thickness and width of the beam were calculated from the FE model, while the same dimensions of the experimental beam were measured. As far as the major trends in variations were concerned, the two sets of data were found to agree. As for the differences observed, some of the reasons were inaccuracies with curve fitting, measurement errors and the presence of friction.

The methodology for the modal analysis of the FE dimpled beam was detailed in Chapter 6. The three-dimensional nature of this model enables it to demonstrate lateral and torsional modes of vibration in addition to transverse modes and makes it a more faithful representation of the experimental dimpled beam. The procedure used to perform an experimental modal analysis was described in Chapter 7. In addition to describing the experiment itself, it highlighted the care to be taken to ensure accurate and reliable data collection.

Comparison of the first five natural frequencies obtained from FEA, BVM and experimental modal analysis was the subject of Chapter 8. Free-free beams with a single dimple, with two dimples facing the same direction and with two dimples pointing in opposite directions were used in this study. First, FEA results were compared with experimental values. With rare exceptions, FEA was found to provide accurate predictions of the frequencies compared. They deviated from the experimental values by less than 2.5%. Hence, it can be concluded that the methodology presented here can be used to gain reliable insights into the natural frequencies of dimpled beams with free boundary conditions at both ends. For the same beams and boundary conditions, comparisons were made between FEA and BVM as well. In every scenario, FEA was found to be far superior to BVM as a means for predicting natural frequencies. FEA results were found to be at least four times more accurate than BVM results.

Having summarized this research, this would be a good place for a suggestion regarding the implementation of the methodology proposed in this research. Some of the prerequisites of building an accurate simulation of a dimpled beam are extensive information about the beam material and a good understanding of its deformation mechanics. Besides, it is expensive in terms of computational power and time invested. Thus, it does not lend itself easily to a quick evaluation of the effect of dimple(s) on the vibrational performance of a beam. Hence, a pilot study using the combined finite element and optimization technique proposed by Alshabtat [5] is recommended. If the results from that study are encouraging, the procedure followed in this research could be used to achieve an in-depth understanding of the way dimple(s) would affect the beam's vibrational performance.

9.2. Future work

This research has led to a better understanding of the effects of stamping on the natural frequencies of dimpled beams. At the same time, it has raised additional questions and opened new avenues for further research. The scope of this future work is presented in subsequent paragraphs.

First, enhancements need to be made to the physical stamping setup. In its present state, its operation is far too uncontrolled and imprecise. It would undoubtedly benefit from some standardization. The addition of a scale to measure the plunger's travel would be a welcome improvement. Additionally, a means to measure the force applied by the plunger would provide insight into the resistance caused by friction. A decrease in this force due to the use of lubrication could also be treated as a measure of the lubricant's effectiveness. Besides, design changes to enable horizontal movement of the clamping blocks would allow the use of varying sizes of the plunger and help create a wider variety of dimples.

Further, the lack of lubrication during stamping introduces considerable friction between the plunger and the beam. This adds an immeasurable element of unpredictability to the mechanics of beam deformation, which makes it hard to replicate in the FE simulation as well. The use of a lubricant has the potential to not only reduce friction substantially, but also its effect on the shape of the dimple. This reduction might even be large enough to allow for much better agreement between the geometries of the FE and experimental beams. The present research added to the knowledge of dimple geometry by noting that both its width and its thickness change along its length. Besides, the thickness of the dimple might vary along the width as well. A study of the causes and effects of this phenomenon might be worthwhile in offering a greater understanding of the effects of stamping. Also, the logical step forward for this research would be to build a similar simulation of the creation of beads and spherical dimples on plates. Ultimately, for this research to be implemented in the real world, a study must be conducted which involves beads and dimples on curved plates.

Manual measurements of the thickness and width of the beam were used to validate the FE structural simulation. Before settling on that method though, the use of a 3-D optical

coordinate measuring technique was proposed. This technique is described in greater depth by Pendse et al. [22]. Although the initial outcome from this method was encouraging, the data collected, and the algorithm used to interpret it produced results that were too inconsistent for the recreation of a cohesive model of the dimpled beam. Consequently, this approach was abandoned in favor of the manual measurements described here. However, improvements could be made to the data collected by the machine vision system and/or the algorithms used to interpret that data. Also, errors in the curve-fitting procedure used to calculate the thickness of the FE beam could be reduced. Instead of fitting a single curve to the whole dimple, fitting a spline to a small local set of points could lead to a better fit. These changes would potentially facilitate a finer comparison of the FE beam with the experimental beam than the one afforded by current methods.

The three-dimensional nature of the simulation presented here allows it to exhibit non-transverse modes of vibration. Physical measurements of these lateral and torsional vibrations would validate that aspect of the model as well and grant extra credibility to its accuracy and robustness. Through this and other enhancements suggested here, it might be possible to refine the simulation to very high standards of accuracy and reliability. That could ultimately allow the complete circumvention of the physical process of stamping and lead to complete reliance on the simulation to predict the vibrational performance of dimpled and beaded structures.

REFERENCES

[1] J. Carneal, F. Charette and C. Fuller, "Minimization of sound radiation from plates using adaptive tuned vibration absorbers," *Journal of Sound and Vibration,* vol. 270, pp. 781-792, 2004.

[2] J. Du and N. Olhoff, "Minimization of sound radiation from vibrating bi-material structures using topology optimization," *Structural and Multidisciplinary Optimization,* vol. 33, pp. 305-321, 2007.

[3] P. Joshi, S. Mulani, S. Gurav and R. Kapania, "Design optimization for minimum sound radiation from point-excited curvilinearly stiffened panels," in *50th AIAA/ASME/ASCE/AHS/ASC Structures, Structural Dynamics, and Materials Conference*, Palm Springs, California, 2009.

[4] K. Naghshineh, Strategies for the optimum design of quiet structures: Use of material tailoring and/or active vibration control, Pennsylvania State University, 1991.

[5] N. Alshabtat, Beading and dimpling techniques to improve the vibration and acoustic characteristics of plate structures, Western Michigan University, 2011.

[6] K. Myers, Analysis of vibroacoustic properties of dimpled beams using a boundary value model, Western Michigan University, 2015.

[7] M. Ghazwani, Development of an analytical model for beams with two dimples in opposing directions, Western Michigan University, 2016.

[8] W. Cheng, C. Cheng and G. Koopmann, "A new design strategy for minimizing sound radiation of vibrating beam using dimples," *Journal of Vibration and Acoustics,* vol. 133, 2011.

[9] GOM mbH, ATOS v5.2.0 Preliminary User Manual, Braunschweig, Germany: GOM mbH, 2003.

[10] ASTM Standard E8/E8M - 16a, *Standard test methods for tension testing of metallic materials,* ASTM International, West Conshohocken, PA, 2016.

[11] A. Ugural and S. Fenster, Advanced strength and applied elasticity, New York, NY: Elsevier North Holland Publishing Company, Inc., 1979.

[12] P. Dixit and U. Dixit, Modeling of metal forming and machining processes by finite element and soft computing methods, London, UK: Springer-Verlag, 2008.

[13] Y. Bai and W. Jin, Marine Structural Design, 2nd edition, Oxford, UK: Butterworth-Heinemann, 2015.

[14] M. Vable, Mechanics of materials, New York, NY: Oxford University Press, 2002.

[15] Matweb, "Properties of AISI 1015 steel," [Online]. Available: http://www.matweb.com/search/DataSheet.aspx?MatGUID=6cd3ff8c19bb42bda1fa848e6d12bbb9. [Accessed 21 November 2019].

[16] American Institute of Physics, American institute of physics handbook, 3rd edition, McGraw-Hill, 1972.

[17] ANSYS, Academic Teaching Mechanical, Release 19.1, Help System, Element Reference, ANSYS, Inc..

[18] D. Montgomery, Design and analysis of experiments, 8th edition, John Wiley and Sons, Inc., 2013.

[19] PCB Piezotronics, PCB test and measurement catalog, PCB Piezotronics.

[20] m+p International, "Dynamic signal analyzer," m+p International, [Online]. Available: https://www.mpihome.com/en/products/dynamic-signal-analysis.html. [Accessed 21 November 2019].

[21] L.-W. Cai, Fundamentals of mechanical vibrations, Chichester, England: ASME Press, 2016.

[22] V. Pendse, M. Ghazwani and K. Naghshineh, "Investigation of the effect of stamping process on dimpled beams," in *ISMA 2018 International Conference on Noise and Vibration Engineering USD 2018 International Conference on Uncertainty in Structural Dynamics*, Heverlee, Belgium, 2018.

Appendix A:

Finite element code for simulation of stamping

The workings of the finite element simulation of stamping are explained in depth in Chapter 4. This appendix provides the program read into ANSYS Parametric Design Language for that purpose. It is in the form of a text (.txt) file and its function is to simulate stamping to create two dimples facing opposite directions on the beam. It is read into the software using the following two lines of code:

/CWD,'Directory path to Multidimp_Static'
/INPUT,' Multidimp_Static',txt

The first line directs the software to the folder where the input file (named 'Multidimp_Static') is located, while the second line instructs it to read the input file. Here, it is presented as a list of commands with an explanation for that command in front of it. The exclamation marks inform the software that the text following it is a comment and not to be executed.

Command	Explanation
/BATCH,LIST	
FINISH	
/CLEAR	
/CWD,'Working directory for the rest of the simulation'	
/FILNAME,Multidimp_Static,1	!Jobname for analysis
/UNITS,SI	!System of units
*SET,PI,3.14159265359	!Value of pi
/PREP7	

!Dimensions	
*SET,RP,15E-3	!Plunger radius
*SET,GAP,1E-3	!Initial gap between the beam and the plunger (also equal to the clearance between the plunger and the die)
SET,LD,2(RP+GAP)	!Dimple chord length
*SET,WC,2*RP	!Width (X-dimension) of the clamp (die block)
*SET,L1,45E-3	!Length of the first straight segment
*SET,L2,65E-3	!Length of the second straight segment
*SET,L3,130E-3	!Length of the third straight segment
*SET,LB,L1+L2+L3+(4*RP)	!Beam length (X-dimension)
*SET,TB0,1.15E-3	!Beam thickness (Y-dimension)
*SET,WB,25.8E-3	!Beam width (Z-dimension)
*SET,ALPHADEG,135/2	!Dimple half-angle in degrees
*SET,ALPHA,(ALPHADEG*PI)/180	!Conversion to radians
SET,HD,RP(1-COS(ALPHA))	!Dimple height (or depth)
*IF,(NINT(10E3*HD))-(10E3*HD),GE,0,THEN	!This *IF block limits the accuracy of calculation of HD to one decimal place by rounding.
*SET,HD,(NINT(10E3*HD))*1E-4	!Load steps defined later on, depend on this value of HD for their numbering.
*ELSE	!Values with more than one decimal place introduce a gap in the numbering leading to error during solution.
*SET,HD,(NINT(10E3*HD)+1)*1E-4	!This tradeoff is relatively insignificant as the rounding errors are an order of magnitude below the individual load step deflections.

*ENDIF	
*SET,PL1_CENTERX,L1+RP	!X coordinate of first plunger's center from the left end of the beam
*SET,PL1_X,PL1_CENTERX-(LB/2)	!X coordinate of first plunger's center in the global coordinate system
*SET,PL1_Y,(TB0/2)+GAP+RP	!Y coordinate of first plunger's center in the global coordinate system (similar for PL2_Y)
*SET,PL2_CENTERX,L1+L2+(3*RP)	!X coordinate of second plunger's center from the left end of the beam
*SET,PL2_X,PL2_CENTERX-(LB/2)	!X coordinate of second plunger's center in the global coordinate system
*SET,PL2_Y,+((TB0/2)+GAP+RP)	!Plus sign indicates both dimples face the same way. Minus sign indicates dimples face opposite ways.
*IF,PL2_Y,GT,0,THEN	!Creation of the SIGN variable facilitates coding for the second dimple regardless of its orientation relative to the first dimple (same or opposite)
*SET,SIGN,+1	
*ELSEIF,PL2_Y,LT,0	
*SET,SIGN,-1	
*ENDIF	
*SET,PL_ANGLE1,0	
*SET,PL_ANGLE2,-180	
ET,1,SOLID187	!Element type for plunger
ET,2,SOLID186	!Element type for beam

NLGEOM,ON	!Non-linear effects ON
!Material properties	
*SET,Young,196E9	!Modulus of elasticity
*SET,Poisson,0.29	!Poisson's ratio (taken from AISI 1015 steel data sheet)
*SET,Friction,0.52	!Coefficient of friction
*SET,Density,7870	!Density (taken from AISI 1015 steel data sheet)
MPTEMP,1,0	!Non-linear material properties
MPDATA,EX,1, ,Young	!Modulus of elasticity
MPDATA,PRXY,1, ,Poisson	!Poisson's ratio
MPDATA,MU,1, ,Friction	!Coefficient of friction
MPDATA,DENS,1, ,Density	!Density
TB,PLASTIC,1, , ,MISO	!Multilinear isotropic hardening behavior
TBTEMP,0	
*SET,NUM_ROWS,7	!Number of rows in the material properties data set being read
*DIM,MATPROPS,ARRAY,NUM_ROWS,2,1	!Reading the stress-strain data into the variable MATPROPS
*VREAD,MATPROPS,'B:\Google Drive\Thesis\Tension testing\Test data\Data analysis\Stress-strain data for ANSYS v3',TXT, ,KJI,1,2,NUM_ROWS	

(2X,E14.7,3X,E13.7)	
*DO,PROPROW,1,NUM_ROWS,1	!Reading the stress-strain data from MATPROPS
TBPT,DEFI,MATPROPS(PROPROW,2),MATPROPS(PROPROW,1)	
*ENDDO	
!FINISH	!These FINISH and /EOF blocks allow code debugging. Uncomment this block to run the code till this point and stop.
!/EOF	!Comment out all of these blocks to run the complete code
CYL4,PL1_X,PL1_Y,RP,PL_ANGLE1,0,PL_ANGLE2,WB	!Modelling the first plunger
CYL4,PL2_X,PL2_Y,RP,PL_ANGLE1,0,SIGN*PL_ANGLE2,WB	!Modelling the second plunger
BLC4,-(LB/2),-(TB0/2),LB,TB0,WB	!Modelling the beam
!FINISH	
!/EOF	
!Forming components for easy access	
ALLSEL	
VSEL,S,LOC,Y,PL1_Y-RP,PL1_Y	!Selecting the first plunger
VSEL,R,LOC,X,PL1_X-(LD/2),PL1_X+(LD/2)	

CM,PLUNGER1,VOLU	!Forming a volume component named 'PLUNGER1'
ALLSEL	
*IF,PL2_Y,GT,0,THEN	!Selecting the second plunger
VSEL,S,LOC,Y,PL2_Y-RP,PL2_Y	
VSEL,R,LOC,X,PL2_X-(LD/2),PL2_X+(LD/2)	
CM,PLUNGER2,VOLU	!Forming a volume component named 'PLUNGER2'
ALLSEL	
*ELSEIF,PL2_Y,LT,0	
VSEL,S,LOC,Y,PL2_Y,PL2_Y+RP	
VSEL,R,LOC,X,PL2_X-(LD/2),PL2_X+(LD/2)	
CM,PLUNGER2,VOLU	
ALLSEL	
*ENDIF	
ALLSEL	
VSEL,S,LOC,Y,-(TB0/2),(TB0/2)	!Selecting the beam
VSEL,R,LOC,X,-(LB/2),LB/2	
CM,BEAM,VOLU	!Forming a volume component named 'BEAM'
ALLSEL	
ALLSEL	!Assigning non-linear material properties to beam and both plungers
VSEL,S, , ,PLUNGER1	
VATT,1,1,1	!Assign element type 1 (SOLID187) to both plungers

ALLSEL	
VSEL,S, , ,PLUNGER2	
VATT,1,1,1	
ALLSEL	
VSEL,S, , ,BEAM	
VATT,1,1,2	!Assign element type 2 (SOLID186) to beam
ALLSEL	
!FINISH	
!/EOF	
!Meshing the model	
AESIZE,PLUNGER1,5E-3	!Element size for PLUNGER1
AESIZE,PLUNGER2,5E-3	!Element size for PLUNGER2
ALLSEL	!Element size for BEAM
LSEL,S, , ,BEAM	
LSEL,R,LENGTH, ,LB,LB	
LESIZE,ALL,TB0, , , ,1, , ,OFF	
ALLSEL	
LSEL,S, , ,BEAM	

LSEL,R,LENGTH, ,TB0,TB0	
LESIZE,ALL,TB0/2, , , ,1, , ,OFF	
ALLSEL	
LSEL,S, , ,BEAM	
LSEL,R,LENGTH, ,WB,WB	
LESIZE,ALL,TB0/2, , , ,1, , ,OFF	
ALLSEL	
ALLSEL	
VMESH,ALL	!Mesh all volumes
ALLSEL	
!FINISH	
!/EOF	
!Setting up contact	
ALLSEL	!DEFINE CONTACT ELEMENTS!! EXTREMELY IMPORTANT!!
ASEL,S, , ,PLUNGER1	!Selecting the plunger side of the contact area between plunger and beam
ASEL,U,LOC,Y,PL1_Y,PL1_Y	
ASEL,U,LOC,Z,0,0	
ASEL,U,LOC,Z,WB,WB	

NSLA,S,1	!Select the associated nodes
CM,PLUNGER1_CONTACT,NODE	!Form a component 'PLUNGER1_CONTACT' from the selected nodes
ALLSEL	!Create the 'PLUNGER2_CONTACT' component by selecting the nodes on the curved face of the second plunger
ASEL,S, , ,PLUNGER2	
ASEL,U,LOC,Y,PL2_Y,PL2_Y	
ASEL,U,LOC,Z,0,0	
ASEL,U,LOC,Z,WB,WB	
NSLA,S,1	
CM,PLUNGER2_CONTACT,NODE	!Form a component 'PLUNGER2_CONTACT' from the selected nodes
ALLSEL	
ASEL,S, , ,BEAM	
ASEL,R,LOC,Y,TB0/2,TB0/2	!Selecting the nodes on the beam side of the contact area between plunger and beam
NSLA,S,1	
CM,BEAM_CONTACT1,NODE	!Form a component from the selected nodes
ALLSEL	!Create the 'BEAM_CONTACT2' component by selecting nodes on the side of the beam where the plunger is present
ASEL,S, , ,BEAM	
ASEL,R,LOC,Y,SIGN*TB0/2,SIGN*TB0/2	
NSLA,S,1	
CM,BEAM_CONTACT2,NODE	
ALLSEL	
ALLSEL	

REAL,3	!Assign real constant set number 3 to the subsequently defined contact and target elements for the first plunger
ET,3,TARGE170	!Selecting target elements (a type of contact elements which will be used for the plunger)
KEYOPT,3,2,1	!User-specified boundary conditions for rigid target nodes
ET,4,CONTA174	!Selecting contact elements (a type of contact elements which will be used for the beam)
KEYOPT,4,1,0	!UX, UY and UZ DOFs
ALLSEL	
NSEL,S, , ,PLUNGER1_CONTACT	!Select the nodal component PLUNGER1_CONTACT
TYPE,3	!Assign element type 3 (TARGE170) to the component PLUNGER1_CONTACT
ESLN,S,0,ALL	!Select associated elements
ESURF	!Generate contact elements on the plunger
ALLSEL	
NSEL,S, , ,BEAM_CONTACT1	!Select the nodal component BEAM_CONTACT1
TYPE,4	!Assign element type 4 (CONTA174) to the component BEAM_CONTACT1
ESLN,S,0,ALL	!Select associated elements
ESURF	!Generate contact elements on the beam
ALLSEL	
REAL,4	!Assign real constant set number 3 to the subsequently defined contact and target elements for the second plunger

ALLSEL	
NSEL,S, , ,PLUNGER2_CONTACT	!Select the nodal component PLUNGER2_CONTACT
TYPE,3	!Assign element type 3 (TARGE170) to the component PLUNGER2_CONTACT
ESLN,S,0,ALL	!Select associated elements
ESURF	!Generate contact elements on the plunger
ALLSEL	
NSEL,S, , ,BEAM_CONTACT2	!Select the nodal component BEAM_CONTACT2
TYPE,4	!Assign element type 4 (CONTA174) to the component BEAM_CONTACT2
ESLN,S,0,ALL	!Select associated elements
ESURF	!Generate contact elements on the beam
ALLSEL	
!FINISH	
!/EOF	
NSEL,S, , ,BEAM	
NWRITE,NodeBefore_full,txt, ,0	!Write a list of nodes' coordinates before the solution
ALLSEL	
!Set the initial boundary conditions and the first load step for the first plunger	

*SET,UY0,0.9*GAP	
ALLSEL	
NSEL,S,LOC,X,PL1_X+(LD+WC)/2,PL1_X+(LD/2)+WC	
NSEL,A,LOC,X,PL1_X-((LD+WC)/2),PL1_X-((LD/2)+WC)	
NSEL,R,LOC,Y,TB0/2,TB0/2	
D,ALL,UY,0, , , ,UX,UZ	!Constraining all DOFs for the top of the beam in the outer half of the clamp (die block)
ALLSEL	
NSEL,S,LOC,X,PL1_X+LD/2,PL1_X+(LD+WC)/2	
NSEL,A,LOC,X,PL1_X-(LD/2),PL1_X-((LD+WC)/2)	
NSEL,R,LOC,Y,TB0/2,TB0/2	
D,ALL,UY,0	!Constraining Y-displacement for the top of the beam in the inner half of the clamp (die block)
ALLSEL	
NSEL,S,LOC,X,PL1_X+LD/2,PL1_X+LD/2	
NSEL,A,LOC,X,PL1_X-(LD/2),PL1_X-(LD/2)	
NSEL,R,LOC,Y,-(TB0/2),-(TB0/2)	!Selecting the points on the bottom of the beam where it is in contact with the die
D,ALL,UY,0	!Constraining Y-displacement of that point
ALLSEL	
ASEL,S, , ,PLUNGER1	
NSLA,S,1	
D,ALL,UX,0, , , ,UZ	!Constraining X-displacement on the plunger

ALLSEL	
ASEL,S, , ,PLUNGER1	
NSLA,S,1	
D,ALL,UY,-UY0	!Initial displacement of the plunger
ALLSEL	
LSWRITE,INIT	!Reset load step file numbering counter to 1
LSWRITE,1	!Save current load setup as load step 1
ASEL,S, , ,PLUNGER1	
NSLA,S,1	
DDELE,ALL,UY	!Delete all displacement in the Y direction (to prevent conflicts when specifying constraints on the same area in the future)
ALLSEL	
!FINISH	
!/EOF	
*SET,Loop1Def,(GAP+HD)-UY0	!Total deformation occuring in the following loop
*SET,UYInc1,0.1E-3	!Deformation increments
*DO,LSt1,2,(Loop1Def/UYInc1)+1,1	!*DO loop for load steps
ALLSEL	
ASEL,S, , ,PLUNGER1	

NSLA,S,1	
D,ALL,UY,-(UY0)-((LSt1-1)*(UYInc1))	!Step-wise loading the Y direction
ALLSEL	
LSWRITE,LSt1	!Write load step file
ASEL,S, , ,PLUNGER1	
NSLA,S,1	
DDELE,ALL,UY	!Delete all displacement in the Y direction (to prevent conflicts when specifying constraints on the same area in the future)
ALLSEL	
*ENDDO	
!FINISH	
!/EOF	
ALLSEL	
*SET,Loop2Def,HD/4	!A loop, similar to the one above, used to lift the plunger up
*SET,UYInc2,0.1E-3	
*DO,LSt2,(Loop1Def/UYInc1)+2,(Loop1Def/UYInc1)+1+(Loop2Def/UYInc2),1	
*SET,Count2,LSt2-((Loop1Def/UYInc1)+1)	
ALLSEL	
ASEL,S, , ,PLUNGER1	

NSLA,S,1	
D,ALL,UY,-(UY0)-(Loop1Def)+((Count2)*(UYInc2))	
ALLSEL	
LSWRITE,LSt2	
ASEL,S, , ,PLUNGER1	
NSLA,S,1	
DDELE,ALL,UY	
ALLSEL	
*ENDDO	
*SET,LStTot1,(Loop1Def/UYInc1)+1+(Loop2Def/UYInc2)	
!Set the initial boundary conditions and the first load step for the second plunger	
ALLSEL	
NSEL,S,LOC,X,PL2_X+(LD+WC)/2,PL2_X+(LD/2)+WC	
NSEL,A,LOC,X,PL2_X-((LD+WC)/2),PL2_X-((LD/2)+WC)	
NSEL,R,LOC,Y,SIGN*TB0/2,SIGN*TB0/2	
D,ALL,UY,0, , , ,UX,UZ	!Constraining all DOFs for the top of the beam in the outer half of the clamp (die block)
ALLSEL	
NSEL,S,LOC,X,PL2_X+LD/2,PL2_X+(LD+WC)/2	

NSEL,A,LOC,X,PL2_X-(LD/2),PL2_X-((LD+WC)/2)	
NSEL,R,LOC,Y,SIGN*TB0/2,SIGN*TB0/2	
D,ALL,UY,0	!Constraining Y-displacement for the top of the beam in the inner half of the clamp (die block)
ALLSEL	
NSEL,S,LOC,X,PL2_X+LD/2,PL2_X+LD/2	
NSEL,A,LOC,X,PL2_X-(LD/2),PL2_X-(LD/2)	
NSEL,R,LOC,Y,-SIGN*TB0/2,-SIGN*TB0/2	!Selecting the points on the bottom of the beam where it is in contact with the die
D,ALL,UY,0	!Constraining Y-displacement of that point
ALLSEL	
ASEL,S, , ,PLUNGER2	
NSLA,S,1	
D,ALL,UX,0, , , ,UZ	!Constraining X-displacement on the plunger
ALLSEL	
ASEL,S, , ,PLUNGER2	
NSLA,S,1	
D,ALL,UY,-SIGN*UY0	!Initial displacement of the plunger
ALLSEL	
LSWRITE,LStTot1+1	!Save current load setup as load step 1
ASEL,S, , ,PLUNGER2	
NSLA,S,1	
DDELE,ALL,UY	!Delete all displacement in the Y direction (to prevent conflicts when specifying constraints on the same area in the future)

ALLSEL	
!FINISH	
!/EOF	
*DO,LSt1,LStTot1+2,LStTot1+(Loop1Def/UYInc1)+1,1	!*DO loop for load steps
ALLSEL	
ASEL,S, , ,PLUNGER2	
NSLA,S,1	
D,ALL,UY,-SIGN*((UY0)+((LSt1-LStTot1-1)*(UYInc1)))	!Step-wise loading the Y direction
ALLSEL	
LSWRITE,LSt1	!Write load step file
ASEL,S, , ,PLUNGER2	
NSLA,S,1	
DDELE,ALL,UY	!Delete all displacement in the Y direction (to prevent conflicts when specifying constraints on the same area in the future)
ALLSEL	
*ENDDO	
!FINISH	
!/EOF	

*DO,LSt2,LStTot1+(Loop1Def/UYInc1)+2,LStTot1+(Loop1Def/UYInc1)+1+(Loop2Def/UYInc2),1	
*SET,Count2,LSt2-(LStTot1+(Loop1Def/UYInc1)+1)	
ALLSEL	
ASEL,S, , ,PLUNGER2	
NSLA,S,1	
D,ALL,UY,-SIGN*((UY0)+(Loop1Def)-((Count2)*(UYInc2)))	
ALLSEL	
LSWRITE,LSt2	
ASEL,S, , ,PLUNGER2	
NSLA,S,1	
DDELE,ALL,UY	
ALLSEL	
*ENDDO	
*SET,LStTot2,LStTot1+(Loop1Def/UYInc1)+1+(Loop2Def/UYInc2)	
!FINISH	
!/EOF	
ANTYPE,STATIC,NEW	!Static analysis
NSUBST,10,500,1,OFF	!Specify the number of substeps to be taken

RESCONTROL,NORESTART,NONE,NONE	!Forcing the 'no restart' option (Sometimes, the solution is inexplicably interrupted because ANSYS 'cannot find the restart file')
!FINISH	
!/EOF	
/SOLU	
LSSOLVE,1,LStTot2,1	!Solve load step files one at a time
!FINISH	
!/EOF	
/PREP7	
NSEL,S, , ,BEAM	
UPCOORD,1	
ALLSEL	
NSEL,S, , ,BEAM	
NWRITE,NodeAfter_full,txt, ,0	!Write a list of nodes' coordinates after the solution
ALLSEL	

SAVE, , , ,ALL	!Save the current database (.db) file (for use in modal analysis)
FINISH	
/EOF	

Appendix B:

Finite element code for modal analysis

This appendix provides the input program for the modal analysis part of the simulation. Its functioning is described in detail in Chapter 6. This code imports the database and results file from the previous stamping simulation. While it can implement fixed-fixed and cantilever boundary conditions on the beam, those lines are commented out in the code below to create free-free boundary conditions. Just like the code for the stamping simulation, this program requires the same two commands to be entered first to direct the software to the input file. It is also presented in a similar tabular format.

Command	Explanation
/BATCH,LIST	
FINISH	
/CLEAR	
/CWD,'Working directory for the rest of the simulation'	
/FILNAME,Multidimp_Modal,1	!Jobname for analysis
/UNITS,SI	!System of units
/PREP7	
UPGEOM,1, , ,'Path to results file\Multidimp_Static',RST	!Restore the results (.rst) file of the previous nonlinear static analysis
RESUME,'Path to database file\Multidimp_Static',DB, ,0	!Restore the database (.db) file of the previous nonlinear static analysis
!FINISH	
!/EOF	
ALLSEL	
VSEL,S, , ,PLUNGER1	!Select the first plunger
VSEL,A, , ,PLUNGER2	!Select the second plunger
VCLEAR,ALL	!Clear the mesh on both plungers

VDELE,ALL, , ,1	!Delete the plungers
ALLSEL	
!FINISH	
!/EOF	
ALLSEL	
ESEL,S,ENAME, ,CONTA174	!Select contact elements
ESEL,A,ENAME, ,TARGE170	!Select target elements
EDELE,ALL	!Delete contact and target elements
ALLSEL	
NDELE,PLUNGER1_CONTACT	!Delete components consisting of the plungers' contact elements
NDELE,PLUNGER2_CONTACT	
ALLSEL	
NUMCMP,ALL	!Reset numbering for all entities after previous deletions
!FINISH	
!/EOF	
ALLSEL	
DDELE,ALL,ALL	!Delete all previous DOF constraints
ALLSEL	
!ALLSEL	!Fixed-fixed end conditions
!NSEL,S,LOC,X,-(LB/2),-(LB/2)	
!NSEL,A,LOC,X,(LB/2),(LB/2)	
!NSEL,R,LOC,Y,-TB0/2,TB0/2	
!D,ALL,UX,0, , , ,UY,UZ	

!ALLSEL	
!ALLSEL	
!NSEL,S,LOC,X,+(LB/2),+(LB/2)	!Cantilever end conditions (Minus sign fixes the left end; plus sign fixes the right end)
!NSEL,R,LOC,Y,-TB0/2,TB0/2	
!D,ALL,UX,0, , , ,UY,UZ	
!ALLSEL	
!FINISH	
!/EOF	
ANTYPE,MODAL,NEW	!New modal analysis
MODOPT,LANB,20,1,100000	!Modal analysis options
MXPAND,20,1,100000,YES	!Number of modes to expand
!FINISH	
!/EOF	
/SOLU	
SOLVE	
FINISH	
/EOF	